1 **Brown carbon in fine particles in four typical cities in North-**

2 **west China during wintertime: coupling optical properties**

3 **with chemical processes**

4

5 Miao Zhong[a,b], Jianzhong Xu[a,*], Huiqin Wang[c], Li Gao[d], Haixia Zhu[e], Lixiang Zhai[a,b],

6 Xinghua Zhang[a], Wenhui Zhao[a,b]

7 [a]State Key Laboratory of Cryospheric Sciences, Northwest Institute of Eco-Environment and Resources,

8 Chinese Academy of Sciences, Lanzhou 730000, China

9 [b]University of Chinese Academy of Sciences, Beijing 100049, China

10 [c]Institute of Desert Meteorology, China Meteorological Administration, Urumqi 830002, China

11 [d]College of Resources and Environment, Ningxia University, Yinchuan 750021, China

12 [e]Key Laboratory of Comprehensive and Highly Efficient Utilization of Salt Lake Resources, Qinghai

13 Institute of Salt Lakes, Chinese Academy of Science, Xining, Qinghai 810008, China

14 *Corresponding to*: Jianzhong Xu (jzxu@lzb.ac.cn)

15

16   **Abstract.** Brown carbon (BrC) aerosol could impact atmospheric radiative forcing and play a crucial

17   role in atmospheric photochemistry. Most previous studies have predominantly focused on bulk optical

18   properties of ambient BrC from biomass burning emitted primary or secondary BrC aerosol. Few studies

19   have focused on fossil-fuel-influenced BrC aerosol, especially coal combustion emissions. In this study,

20   fine particulate matter ($PM_{2.5}$) filter samples were collected synchronously in four capital cities of North-

21   west China during the winter season (December 2019–January 2020): Lanzhou (LZ), Xining (XN), Yin-

22   chuan (YC), and Urumqi (UR), which are represented as energy-producing and heavy manufacturing

23   cities in China. The aim of the study was to explore the optical properties, sources, and chemical pro-

24   cesses of water-soluble BrC (WS-BrC). The average mass absorption efficiency at 365 nm (MAE365)

25   of WS-BrC at these four cities were 1.24 ± 0.19 m^2/g (XN), 1.19 ± 0.12 m^2/g (LZ), 1.07 ± 0.23 m^2/g

26   (YC), and 0.78 ± 0.16 m^2/g (UR), respectively. The properties of WS-BrC were investigated by an acid-

27   base titration experiment. The MAE365 values in all cities increased with increasing pH values (2–11),

28   while the fluorescent intensities of water extracts fluctuated with corresponding pH values, being

29   stronger at higher acidic and basic conditions. The WS-BrC at YC and LZ were the two most sensitive

30   sites to pH variation, suggesting the important contribution of acid/base functional groups. Furthermore,

31   significant photo-enhancement (LZ) or photo-bleaching (YC and UR) phenomena based on coupling

32   bulk chemical properties with light absorption properties were observed in different cities, indicating

33   their sources and/or chemical processes were different among each other.

34

35   The sources and chemical processes of WS-BrC were further explored by the combination of parallel

36   factor analysis (PARAFAC) on excitation-emission matrix of WS-BrC and positive matrix factorization

37   analysis (PMF) on high-resolution mass spectra of water-soluble organic aerosol (OA). Six PARAFAC

38   components including three humic-like substances (LO-HULIS, HO-HULIS1, and HO-HULIS2), two

39   protein-like (PLS) or phenol-like substances, and one undefined substance were obtained. Four PMF

40   factors including a water-soluble primary OA (WS-POA), a less oxidized oxygenated OA that associated

41   with coal combustion-induced WSOA (LO-OOA), and two highly oxidized oxygenated OAs respec-

42   tively from photochemical oxidation and aqueous-phase oxidation transformations (HO-OOA1 and HO-

43   OOA2) were identified. WS-POA was the most important source of light absorption accounting for 30%–

44   60% based on multiple linear regression model and was significantly correlated with PLS and LO-HULIS

45   components. The loss of light absorption of WS-POA is accomplished by conversion to LO-OOA and

46   HO-OOAs through photo- or aqueous reactions, where HO-OOAs were significantly correlated with

47   HO-HULIS component. The potential precursors and reaction pathways for WS-BrC in each city are

48   proposed.

1. Introduction

Brown carbon (BrC) is a certain fraction of organic aerosols that absorb lights in the ultraviolet and visible (UV−Vis) ranges (Andreae and Gelencsér, 2006; Laskin et al., 2015). The light absorption of BrC displays a strong wavelength-dependence which can be characterized by higher value (≥ 2) of the absorption Ångström exponent (AAE) (Laskin et al., 2015). The significant effects of BrC on climate and atmospheric chemistry have been characterized previously. Wang et al. (2018) estimate the global mean absorption direct radiative effect (DRE) of BrC is +0.048W/m^2 using the GEOS-Chem chemical transport model. The absorption of solar radiation due to BrC can also affect the formation of ozone and radicals of •OH/•HO$_2$ and corresponding atmospheric chemical reactions (Mok et al., 2016; Baylon et al., 2018).

Biomass combustion is a major global source of primary BrC, as biomass is widely used for residential heating, cooking, and is also produced during wildfires (Washenfelder et al., 2015; Lin et al., 2017; Zeng et al., 2020). In addition to primary sources, secondary BrC is formed through various reaction pathways related to biomass burning, such as aqueous oxidation of phenolic compounds or gas-phase photo-oxidation of aromatic volatile organic compounds (VOCs) (Lin et al., 2015; Vidovic et al., 2018; Liu et al., 2019; Vidović et al., 2020). The chemical compositions and light absorption of BrC can vary significantly due to atmospheric aging. For instance, BrC can photobleaching through photolysis reactions in the presence of •OH radical and O$_3$, or darken via the formation of nitrated organic compounds (Lin et al., 2015; Zhao et al., 2015; Moise et al., 2015; Li et al., 2020a). Furthermore, atmospheric conditions such as changes in pH, air temperature, and relative humidity can affect the light absorption characteristics of BrC (Song et al., 2013; Moise et al., 2015; Phillips et al., 2017; Qin et al., 2020).

Various optical instruments are used to determine the light absorption of BrC. These instruments include direct measurement of airborne aerosol (e.g., particle soot absorption photometer, photo-acoustic spectroscopy, and cavity ring-down spectroscopy) (Laskin et al., 2015) or offline measurement of aerosol extracts by UV-Vis spectrometer (Hecobian et al., 2010). Excitation-emission matrix spectroscopy (EEMs) was recently used to reveal similar chemical structures and photochemical features, as well as

78   to trace the sources of BrC chromophores (Chen et al., 2016; Tang et al., 2020). A few recent studies

79   have characterized BrC compounds by combining high-resolution mass spectrometry and UV-vis spec-

80   troscopy (Lin et al., 2015; Lin et al., 2016; Lin et al., 2018; Wang et al., 2019; Huang et al., 2020; Ni et

81   al., 2021), which facilitates the assessment of the chemical composition of BrC chromophores at the

82   molecular level. For instance, Xu et al. (2020b) discovered that the light absorption of water-soluble

83   organic carbon (WSOC) in the southern regions of TP is higher than that in the northern regions of TP,

84   as well as a considerable variation in the molecular composition of WSOC at two regions.

85

86   In China, coal is still a primary source of energy due to its extensive use in coal-fired power plants,

87   industrial steam boilers, and central heating during winter (Zhang et al., 2008; Yang et al., 2020b). It is

88   particularly prevalent in Western China, where numerous industrial bases have been established since

89   the Development of China's Western Regions strategy in the 2000s. In recent years, cities in Northwest

90   China have experienced more severe air pollution due to rapid economic development and intensive

91   anthropogenic activities, especially in the capital cities of this region. Some recent studies have identified

92   coal combustion as a significant source of BrC in Northwest China (Tan et al., 2016; Chen et al., 2021;

93   Zhang et al., 2021a). Compared with BrC resulting from biomass burning, the optical and chemical prop-

94   erties of BrC emitted from coal combustion have not been well-characterized.

95

96   The aim of this study is to characterize the optical properties of water-soluble BrC (WS-BrC) by collect-

97   ing $PM_{2.5}$ filter samples from four capital cities in Northwest China and analyzing them using a suite of

98   instruments. In particular, the study focused on the contribution of primary and secondary sources of

99   atmospheric chromophores and the related chemical processes. This was achieved by combining data

100 from Excitation-Emission Matrices (EEMs) and High-Resolution Aerosol Mass Spectrometry (HR-

101 AMS).

102

103 **2. Methods**

104 2.1. Filter samples collection at the four cities

105

106 $PM_{2.5}$ filter samples were collected synchronously from four capital cities in Northwest China, namely

107   Yinchuan (YC), Xining (XN), Urumqi (UR), and Lanzhou (LZ), from 5th December 2019 to 20th Janu-

108   ary 2020 (Figure 1). A total of 14 filter samples were collected from each city twice a week. The sam-

109   pling site, located in the cultural and educational districts of each city, were on the rooftops of buildings

110   above 20 meters from the ground and free from significant pollution sources. A medium volume $PM_{2.5}$

111   air sampler (Laoying Ltd., Qingdao, model 2030) with a flow rate of 100 L/min was used for collecting

112   samples in YC (sample IDs: 1−14), while low volume PM2.5 air samplers (Wuhan Tianhong Instrument

113   Co. LTD, TH-16E) with a flow rate of 16.7 L/min and BGI PQ200 low-flow rate aerosol samplers (Mesa

114   Labs, Butler, NJ, USA) were used to collect samples in XN and UR (sample IDs: 15−28 and IDs: 29–

115   42), and LZ (sample IDs: 43−56), respectively. Quartz filters of 90-nm diameter (Whatman, UK) were

116   used for sampling in YC, while in the other three cities, quartz fiber filters of 47-mm diameter (PALL

117   Life Sciences, USA) were used. Before sampling, quartz filters were roasted at 550 °C for five hours to

118   remove carbonaceous particles. Blank filter samples were obtained from each site by leaving the filters

119   in the sampler for ten minutes without sampling. Each filter was wrapped in aluminum foil and frozen at

120   −20 °C until analysis. Daily average concentration of $PM_{2.5}$, SO_2, NO_2, CO, O_3, and meteorological data

121   (air temperature and relative humidity) were obtained from the nearest station of the National Environ-

122   mental Monitoring Net sites (http://www.cnemc.cn/) for comparison. Figure 1 also illustrates the energy

123   consumption structure of industrial enterprises at the four cities, with YC, UR, LZ being energy produc-

124   tion cities, and XN being a heavy manufacturing city (Shan et al., 2018). The energy consumption data

125   for 2019 was obtained from the Statistical Yearbook sharing platform (https://www.yearbookchina.com/).

126

127   2.2. Chemical analysis

128

129   The chemical components of the samples were analyzed using multiple instruments. Firstly, a piece of

130   each filter (0.5024 cm^2) was analyzed for organic carbon (OC) and elemental carbon (EC) contents using

131   a Thermal/Optical carbon analyzer (DRI Model 2015A, Desert Research Institute, USA) with the

132   IMPROVE-A method (Chow et al., 2007). One-quarter of the YC filter and one-half of the other three

133   city filters were extracted in 30ml Milli-Q water (18.2 M Ω·cm) using an ultrasonic bath for 40 minutes.

134   To minimize chemical reactions and evaporation loss during sonication, ice was added to the ultrasonic

135   bath. Water-insoluble residuals were eliminated by filtering extracts via a 0.45-μm PTFE syringe filter

136   (Pall Life Sciences, USA). The concentrations of water-soluble inorganic ions (WSIs) (Cl⁻, NO₃⁻, SO₄²⁻,

137   NH₄⁺, Na⁺, K⁺, Ca²⁺, and Mg²⁺) in the water extracts were analyzed using two 881 compact ion chroma-

138   tography systems (Metrohm, Herisau, Switzerland). The instrument and operation details can be found

139   elsewhere (Xu et al., 2015). WSOC was analyzed using a TOC analyzer (Elementar Vario TOC cube,

140   Hanau, Germany) with the method of total inorganic carbon (TIC) subtracted from total carbon (TC) (Xu

141   et al., 2015; Zhang et al., 2017).

142

143   2.3. Analysis by ultraviolet-visible absorption spectroscopy

144

145   Absorption spectra of water extracts in the 200–700 nm wavelength range were obtained using a UV-

146   visible absorption spectrophotometer (UV-2700; Shimadzu, Kyoto, Japan) at 1 nm intervals with Milli-

147   Q water as the reference. The absorption spectra were corrected by subtracting the absorbance at each

148   wavelength from the average absorption values between 690–700 nm (A_{700}).

149

150   The light absorption coefficient at a given wavelength (Abs_λ) of water extracts was calculated as follows:

151    $$Abs_\lambda = (A_\lambda - A_{700}) \cdot \frac{V_l}{V_a \cdot l} \cdot \ln(10) \qquad (1)$$

152   where A_λ is the absorbance at wavelength λ; V_l is the extract volume (30 mL), V_a is the volume of air

153   passing through the filter, and l is the optical path length, 1 cm.

154

155   The mass absorption efficiency (MAE_λ m²/g) of water extracts and their wavelength dependence of

156   light absorption can be derived as follows:

157    $$MAE_\lambda = \frac{Abs_\lambda}{C_{WSOC}} \qquad (2)$$

158    $$MAE_\lambda = K \cdot \lambda^{-AAE} \text{ (330nm} \leq \lambda \leq \text{400nm)} \qquad (3)$$

159   where K is a constant related to light absorption, and C_{WSOC} is the mass concentration of WSOC (mg/L)

160   in the extract. For simplicity, the absorption at 360–370 nm (mean 365 nm) was used to characterize the

161   absorption of BrC (Hecobian et al., 2010).

162

163   The radiative forcing of WS-BrC relative to EC (f_{BrC}) was estimated as follows (Kirillova et al., 2014):

164

$$f_{BrC} = \frac{\int I_{(\lambda)} \cdot \left\{1 - e^{-\left(MAE_{WSOC,365} \cdot \left(\frac{365}{\lambda}\right)^{AAE_{WSOC}} \cdot \, [WSOC] \, \cdot h_{ABL}\right)}\right\} d\lambda}{\int I_{(\lambda)} \cdot \left\{1 - e^{-\left(MAE_{EC,550} \cdot \left(\frac{550}{\lambda}\right)^{AAE_{EC}} \cdot \, [EC] \, \cdot h_{ABL}\right)}\right\} d\lambda} \tag{4}$$

165 Where [EC] was the mass concentration of EC ($\mu g/m^3$); I(λ) was the clear-sky Air Mass 1 Global Hor-

166 izontal (AM1GH) solar radiance spectrum; $MAE_{EC,550}$ set to 7.5 m^2/g; h_{ABL} refers to the atmospheric

167 boundary layer(1000m); the details are described elsewhere (Kirillova et al., 2014; Bosch et al., 2014).

168

169 2.4. EEM fluorescence spectra analysis

170

171 The three-dimensional excitation-emission matrix spectroscopy (EEMs) of the samples were obtained

172 using an F-7100 fluorescence spectrometer (Hitachi High-Technologies, Japan). The EEMs were meas-

173 ured in the range of 200 to 400 nm with 5 nm intervals for excitation and 250 to 550 nm with 1 nm

174 intervals for emission. The inner filter effect was reduced by diluting the extracts until their absorbance

175 was below 0.1 at 254 nm (Ohno, 2002). The original EEMs were processed following : (1) subtracting

176 the Milli-Q water spectrum to reduce background influence; (2) interpolating to eliminate the interfer-

177 ence signals of the Rayleigh scattered light; (3) adjusting the fluorescence intensity by dividing the Ra-

178 man peak area of Milli-Q water at Ex=350 nm to remove instrument dependency (Lawaetz and Stedmon,

179 2009).

180

181 The resulting fluorescent intensity (unit of RU) was further processed using parallel factor analysis

182 (PARAFAC) to group potential similar chemical components. This was done using the MATLAB 2016b

183 software combined with the DOMFluor and drEEM toolboxes (Murphy et al., 2013). The 6-component

184 model was eventually chosen from 2–10 component PARAFAC models because the residual errors de-

185 creased markedly when the number of components increased from 2 to 6 (Figure S1). In addition, the 6-

186 component model has sensible spectrums of fluorescent components.

187

188 Furthermore, the fluorescence properties of the water extracts were examined through the fluorescence

189 indices. The humification index (HIX) was calculated by the ratio of the integrated fluorescence emission

190 intensity in the region of 435–480 nm to 300–345 nm under the excitation wavelength of 255 nm. The

191   biological index (BIX) was calculated by the ratio of the emission intensity of 380 nm to 430 nm under

192   the excitation wavelength of 310 nm (Zsolnay et al., 1999; Mcknight et al., 2001; Yang et al., 2020b).

193   The average fluorescence intensities (AFI) were calculated in the region of 200–400 nm for excitation

194   wavelengths and 250–550 nm for emission wavelengths.

195

196   The apparent fluorescence quantum yields (AQY) were calculated as follows:

197 $$AQY_\lambda = \frac{\int FI(\lambda_{Ex}, \lambda_{Em}) d\lambda_{Em}}{UVA(\lambda_{Ex}) \int d\lambda_{Em}}\bigg|_{Ex} \qquad (5)$$

198   Where FI represents the fluorescence intensity (RU) at each excitation (200–400 nm) and emission (250–

199   550 nm) wavelength.

200

201   2.5. pH titration experiment

202

203   To investigate the variation of light-absorbing and fluorescent properties of ambient aerosols under the

204   influence of pH, we selected samples with higher WSOA concentrations at each site and recorded their

205   UV-vis absorption and fluorescence spectra at different pH settings. We adjusted the water extracts to pH

206   2 using 2 M HCl and then titrated with 0.1 M NaOH to different pH values until the pH reached 12, as

207   measured by a pH meter (Orion Star A111, Thermo Fisher Scientific, Waltham, MA, USA). We calibrated

208   the pH meter with buffer solutions of pH 4.01, 7.00, and 10.01 during the measurement.

209

210   2.6. HR-AMS Measurements

211

212   Offline high-resolution time-of-flight aerosol mass spectrometry (HR-AMS) was used to analyze the ion-

213   group, elemental ration, and oxidation properties of water-soluble organic aerosol (WSOA). Each water

214   extract was atomized with argon (purity: 99.9999%) to eliminate interference from CO_2 in the air. The

215   generated aerosol was passed through a silica gel diffusion dryer to remove water vapors, and the aerosol

216   particles were then sampled into an HR-AMS instrument (Aerodyne Inc., Billerica, MA, USA) through

217   an aerodynamic lens inlet. The HR-AMS was operated in V- and W-mode. After each sample, deionized

218   water samples were used to clean the sampling line and analyzed as the blank sample using the same

219   procedures. Elemental ratios, including O/C, H/C, N/C, and OM/OC, were determined based on high-

220   resolution mass spectra (m/z up to 120) and the Improved-Aiken (I-A) method (Canagaratna et al.,

221   2015). The elemental contributions of C, O, H, and N reported are mass-based, and more details can be

222   found elsewhere (Xu et al., 2013). Positive matrix factorization (PMF) was performed on high-resolution

223   mass spectra of organics at four cities to identify the potential source factors of WSOA, and four factors

224   were ultimately decomposed. A detailed description of PMF can be found in Zhao et al. (2022).

225

226   In addition, the mass concentration of WSOA were calculated as follows:

227    $$WSOA = \mathrm{WSOC} \cdot \mathrm{OM/OC} \qquad\qquad (6)$$

228

229   **3. Results and discussions**

230   3.1. Overview of the field observations

231

232   Figure 2 presents an overview of the time series of meteorological conditions (air temperature, relative

233   humidity (RH), and precipitation), Abs_{365}, AFI, as well as the mass concentrations of WSIs, WSOA, and

234   EC in the four cities. The weather during the study was generally sunny, cold, and dry (Figure 2a). For

235   instance, the average daily air temperature was -3.2 ± 3.4 °C at YC, -4.4 ± 2.2 °C at XN, -9.2 ± 3.7 °C

236   at UR, and -3.8 ± 2.5 at LZ, and the average RH was $62.4 \pm 15.8\%$ at YC, $56.1 \pm 14.7\%$ at XN, and 58.1

237    $\pm 9.7\%$ at LZ. At UR, there were relatively higher RH condition ($83.9 \pm 6.6\%$), frequent foggy weather,

238   and two significant snowfall events, mainly due to the cold and wet air mass from Arctic Ocean during

239   winter (Yang et al., 2020a). Both the cold/wet and cold/dry weather conditions in our study facilitated

240   the study on different chemical processes.

241

242   The mass concentrations of chemical species in $PM_{2.5}$, as well as their mass fractions of all species varied

243   dynamically during the sampling period in four cities (Figure 2c and 2d). Heavy pollution (defined as

244   the daily average $PM_{2.5}$ mass concentration higher than 150 µg m^{-3}) occurred frequently in UR and fol-

245   lowed by YC (Figure 1). For example, the samples ID of 10–13 and 36–40, both occurred under meteor-

246   ological conditions with high RH condition (Figure 2a and 2c), which were favorable for the secondary

247   generation of atmospheric particulate matters (Sun et al., 2013). Therefore, the contribution of secondary

248   inorganic ions (SNA: sulfate + nitrate + ammonium) showed an important contribution to the recon-

249   structed $PM_{2.5}$ mass (WSOA + EC + WSIs) with an average value of $53.0 \pm 12.7\%$, $41.6 \pm 11.5\%$, 67.3

250    $\pm 7.8\%$, and $41.8 \pm 7.3\%$, respectively, in YC, XN, UR, and LZ, and could be as high as 65.6–76.9%

251   during heavy pollution period at YC and UR (Figure 2d). WSOA was also a major component of $PM_{2.5}$

252   accounting for $31.4 \pm 5.5\%$, $40.6 \pm 5.4\%$, $21.8 \pm 4.6\%$, and $37.7 \pm 4.1\%$ at YC, XN, UR, and LZ, respec-

253   tively. The mass concentration of EC contributed comparably at each city (5.8–8.9%). The higher con-

254   tribution of SNA at YC and UR, in contrast with the higher contribution of WSOA at XN and LZ, likely

255   suggests their different sources and chemical processes. Comparing with the results in literatures, the

256   contributions of WSOA and SNA at XN and LZ in our study are comparable with those in Xi'an, another

257   megacity in Northwest China, during wintertime (Huang et al., 2014), while YC and UR are more com-

258   parable with those cities in East China, such as Beijing, Tianjin, and Jinan, where there are relatively wet

259   condition during wintertime (Lei et al., 2021; Zhang et al., 2021c; Dao et al., 2022). Specially, the chem-

260   ical composition of $PM_{2.5}$ at UR during heavy polluted periods is highly consistent with Beijing (Sun et

261   al., 2020), and the Yangtze River Delta cities during haze episodes (Ge et al., 2017; Ye et al., 2017; Sun

262   et al., 2022).

263

264   The ratio of WSOC/OC is commonly used to predict the potential contribution of secondary organic

265   aerosol to total organic aerosol (Psichoudaki and Pandis, 2013). Overall, WSOC showed a strong corre-

266   lation with OC ($R^2 = 0.84$) with a linear slope of 0.55 for all samples from four cities (Figure S3). The

267   slope values varied among the cities, with YC and UR having higher values (0.61 and 0.59) than XN and

268   LZ (0.54 and 0.52), suggesting a potentially higher secondary OA formation in YC and UR. The

269   WSOC/OC values in our study are within the range reported in other cities during winter, such as Xi'an

270   (0.50 and 0.53) (Zhang et al., 2018; Liu et al., 2020), Beijing (0.74) (Ni et al., 2022) and Guangzhou

271   (0.71) (Tao et al., 2022). Significant correlations among WSOC, OC, EC, Cl^-, K^+ and SNA were found

272   in four cities, indicating similar sources of primary and secondary species (Figure S2, Table S3). Fur-

273   thermore, the light-absorption and fluorescence parameters (Abs_{365} and AFI) followed the variations of

274   WSOC, and we observed significant correlation between them ($R^2_{Abs\ Vs.\ WSOC} = 0.87$; $R^2_{AFI\ Vs.\ WSOC} =$

275   0.61). These findings suggest indicating an important contribution of WS-BrC chromophores to WSOC.

276

3.2. Bulk optical properties of WS-BrC

Figure 3a presents the average MAE spectra of WSOA from various cities. XN and LZ exhibited significantly higher MAE_{365} values (on average 1.22 ± 0.18 and 1.19 ± 0.12 m^2/g) compared to YC (1.02 ± 0.23 m^2/g) and UR (0.78 ± 0.16 m^2/g) (t-test, P < 0.01) (Table 1). The difference in MAE_{365} values among the cities could be attributed to the chemical composition and/or oxygenation state of BrC (Chen et al., 2018; Chen et al., 2020b). When compared with previous studies in other typical Chinese cities during wintertime, the MAE_{365} values in our four cities were lower than those in Xi'an (1.33 and 1.50 m^2/g) (Huang et al., 2018; Yuan et al., 2020). However, the MAE_{365} in XN and LZ were comparable to those of Beijing (1.21–1.26) (Du et al., 2014; Cheng et al., 2016; Li et al., 2020b), while the MAE_{365} in YC were close to those of southern cities in China, such as Guangzhou (0.93 ± 0.06 m^2/g), Nanjing (1.04 m^2/g) (Fan et al., 2016; Chen et al., 2018). Moreover, the MAE_{365} in UR was similar to that of Yangzhou (0.75 ± 0.29 m^2/g) (Chen et al., 2020b).

AAE denotes the wavelength dependence of light absorption of BrC, an important optical parameter that can be used to infer the chemical properties of BrC (Andreae and Gelencsér, 2006). In this study, we found that the AAE values in YC, XN, and UR were 6.8 ± 0.7, 7.1 ± 0.4, and 6.9 ± 0.3, respectively. We observed significantly lower AAE values (6.4 ± 0.5) in LZ (t-test, P < 0.01) (Table 1). Our AAE values fall within the range of values reported in other cities during winter for PM$_{2.5}$ water extracts calculated in the same wavelength range, such as in Nanjing (6.8) (Chen et al., 2018), Beijing (7.3 and 7.5) (Du et al., 2014; Cheng et al., 2016), and Guangzhou (6.7 ± 0.1) (Fan et al., 2016). Previous studies have suggested that higher AAE values may be associated with primary biomass combustion emissions and/or SOA formation. For instance, Chen and Bond (2010) emphasized that particles from smoldering of various wood have largely values between 7–16. Lambe et al. (2013) indicated that secondary BrC generated by laboratory also has a higher AAE value (5.2–8.8). Therefore, the differences in AAE values among the four cities may indicate their different sources or/and chemical compositions.

Saleh (2020) proposed an optical-based classification of BrC using the space of MAE_{405} vs. AAE, which is linked with their physicochemical properties (i.e., molecular sizes and solubility) and atmospheric

306   aging (i.e., photo-enhancement or photo-bleaching). Almost all samples in this study fell into the region

307   of W-BrC, which is similar to ambient samples from other studies (Zhou et al., 2021; Xu et al.,

308   2022). However, a few samples at UR fell into the region of VW-BrC. Furthermore, the WS-BrC in YC

309   exhibited a broader range than other cities, indicating multiple sources and/or processes for WS-BrC in

310   this city. Higher AAE and MAE_{405} values were found in XN, which could be associated with biomass

311   burning emissions. Additionally, WS-BrC in LZ was the closest to the region of M-BrC among the four

312   cities, and the different positions could be related to their chemical processes in each city. For instance,

313   upon examining the relationship between MAE_{365} and the O/C ratio, a positive correlation was observed

314   only in LZ, while negative relationships were observed in other cities (Figure 10). The chemical

315   processes of WS-BrC are discussed in detail in section 3.7.

316

317   The radiative forcing of WS-BrC relative to EC in the wavelength range of 300−2500 nm ($f_{300-2500}$) was

318   found to be 7.05 ± 2.61% at LZ, followed by 5.91 ± 2.54% at XN, 5.10 ± 2.33 at YC, and 3.76 ± 1.53 at

319   UR. The relative radiative effect of WS-BrC in the ultraviolet wavelengths ($f_{300-400}$) was also calculated,

320   accounting for 32.78 ± 7.95%, 29.74 ± 7.15%, 25.45 ± 7.62%, and 18.66 ± 6.17% of EC for LZ, XN,

321   YC, UR, respectively (Table 1). These results indicate that the contribution of the light-absorbing effect

322   from WS-BrC cannot be ignored, particularly in the UV range. The radiative effects of WS-BrC in our

323   study were similar to those in Xi'an (4.99 ± 1.23% for $f_{400-700}$ and 25.9 ± 5.47% for $f_{300-400}$) but lower

324   than those in eastern cities, such as Beijing (10.7 ± 3.0% for $f_{300-2500}$ and 42.2 ± 12.8% for $f_{300-400}$) and

325   Tianjin (13.5 ± 4.1% for $f_{280-4000}$ and 54.3 ± 16.9% for $f_{300-400}$) and Nanjing (9.6% for $f_{300-2500}$ and 39.7%

326   for $f_{300-400}$) (Yan et al., 2015; Liu et al., 2020; Xie et al., 2020; Deng et al., 2022). This difference may be

327   related to the higher light-absorbing effect from BC due to energy-intensive industries and central heating

328   in winter in northwestern cities.

329

330   3.3. Fluorescence Indices

331

332   Fluorescence indexes, such as HIX and BIX, have been used in recent years to study the source and

333   chemical processes of atmospheric organic aerosols (Lee et al., 2013; Fu et al., 2015; Qin et al., 2018;

334   Deng et al., 2022). The HIX indicates the humification of WSOA, and it increases significantly upon

335   aging (Lee et al., 2013; Fan et al., 2020). The BIX is broadly in contrast with HIX and is known as the

336   freshness index. A higher BIX value implies a higher contribution of freshly released organics, while a

337   lower value indicates greater degrees of aging (Lee et al., 2013; Wen et al., 2021).

338

339   Table 1 shows that the HIX and BIX values were 1.85 ± 0.36 and 1.28 ± 0.14 at UR, 1.32 ± 0.23 and

340   1.48 ± 0.11 at YC, 1.29 ± 0.27 and 1.49 ± 0.15 at XN, and 1.16 ± 0.18 and 1.52 ± 0.11 at LZ, respectively.

341   The highest HIX value and lowest BIX value are found in UR, indicating a higher degree of

342   aging/oxidation of WS-BrC. On the other hand, the lower HIX and higher BIX values observed in LZ

343   suggest a high contribution of freshly emitted BrC. These results are consistent with the results of the

344   MAE_{365} discussed earlier.

345

346   The HIX displays a significant negative relationship with BIX for all the data ($R^2 = 0.86$, slope $= 2.19$)

347   (Figure 4a). Figure 4b shows a comparison of our results with other datasets from laboratory or ambient

348   aerosols in different cities in China. All the datasets can be roughly grouped into three zones colored by

349   the grey, pink, and blue dashed boxes, respectively. The freshly introduced materials generated from the

350   laboratory (gray box) are located in a much lower position than those of ambient samples. Differences

351   also exist in ambient samples with our samples (pink box) generally having higher (lower) BIX (HIX)

352   values than those from Eastern China (blue box) (Qin et al., 2018; Yue et al., 2019; Wen et al., 2021;

353   Deng et al., 2022), suggesting that our samples are generally less aged than those from Eastern cities,

354   although the position of UR locates in the overlapped range between these two zones.

355

356   3.4. Influence of pH on optical properties

357

358   Recent studies have shown that the optical properties of BrC vary depending on pH, which is important

359   for modeling its climate-forcing effect, as the general assumption of neutral state for aerosol in models

360   may not be accurate (Phillips et al., 2017). We investigated the effect of pH on the absorption and

361   fluorescence spectra of WSOA in our samples (Figures 5 and 6). The absorption spectra showed a

362   significant increase in absorbance with the increasing pH values (from 2 to 10), with the integrated

363   absorbance (300–450 nm) increased by 66.6%, 55.2%, 43.4%, and 25.3% relative to the pH = 2 level,

364   respectively, in YC, LZ, XN, and UR (Figure S4). The MAE_{365} also increased with increasing pH values

365   (slope = 0.03–0.07), while the AAE decreased (slope = –0.15 to –0.40) (Figure S5). Specifically, the light

366   absorption spectra in YC were the most sensitive to pH variation, followed by LZ, XN, and UR, based

367   on these two slopes. The variations of light absorbance at a function of pH have been observed by

368   previous studies and were attributed to the protonation/deprotonation of carboxyl/phenolic functional

369   groups and/or their variation of macromolecular conformation (Lin et al., 2017; Phillips et al., 2017; Xu

370   et al., 2020b; Qin et al., 2020; Qin et al., 2022a). The different sensitivity of WS-BrC to pH at our

371   sampling sites suggests variations in chemical compositions among them, which could be further

372   investigated through fluorescence spectra.

373

374   The EEM spectra variations upon pH showed the highest values of fluorescent intensity at pH = 2 and

375   tended to decrease with increasing pH. However, for the YC and UR samples, the fluorescent intensity

376   at pH = 10 slightly increased compared to that at pH = 7 (Figure 6). The background mechanism of the

377   fluorescence variation on pH could be related to the rigid properties of fluorophores. The formation of

378   hydrogen bonds at low pH could give special chemical aggregates a stronger rigid planar conformation

379   and enhance fluorescence efficiency (Ghosh and Schnitzer, 1981; Mei et al., 2009). As the pH value

380   increases, the resulting anions repel each other with hydrogen bonds being broken, leading to a more

381   open conformation. This increase in conformational flexibility enhances light absorption but depresses

382   fluorescence. These explains why the light absorbance of WSOC increases under basic conditions, while

383   the fluorescence intensity increases under acidic conditions. In addition to being influenced by

384   conformation, the change in fluorescence spectra of chemical complexes with pH can also result from

385   charge transfer from special acidic/basic groups (Phillips and Smith, 2015; Phillips et al., 2017; Qin et

386   al., 2020). For the results in YC and UR (Figure 7), the fluorescence intensity spectra showing turning

387   points at pH2–4 and pH7–10, could be related to groups of –COOH and–NH_2 and/or –OH, respectively

388   (Cox et al., 1999; Milne et al., 2001; Phillips et al., 2017).

389

390   To identify the potential dominat chemical components of WS-BrC responsible for the pH-dependent

391   variations, the fluorescence peaks in EEM spectra related to special chemical compositions were

392   analyzed for their variations at different pH values (Chen et al., 2003; Fellman et al., 2010). These peaks

393   including peak A (Ex/Em = 225–250/356–440 nm), classified as humic-like fluorophores (Fu et al., 2015;

394   Qin et al., 2018), peak T (Ex/Em = 270–280/330–355 nm), and peak B (Ex/Em = 270–280/290–310 nm),

395   classified as protein-like fluorophores (Chen et al., 2003; Birdwell and Engel, 2010), and peak M (Ex/Em

396   = 310–320/380–420 nm), categorized as oxygenated organic substances (Chen et al., 2003; Qin et al.,

397   2022b). Overall, peak A dominated the variation, contributing 78.5%, 69.1%, 74.1%, and 61.2% of the

398   total variation of all fluorescence peaks in YC, XN, UR, and LZ, respectively. Other peaks showed

399   moderate variations in the four cities, ranging from 8.3% to 12.4% for peak M, 11.2% to 17.9% for peak

400   T, and 1.6% to 7.6% for peak B. The variation trend of peak A was highly consistent with the trends of

401   the average fluorescence efficiency (AFI/TOC) and the average apparent quantum yield (AQY) over the

402   entire Ex/Em range at each city (Figures 7 and S7). These results suggest that the major fluorephores in

403   all the samples are humic-like compounds. Note that although the dominated contribution is from humic-

404   like compound (Peak A) in all the samples, the chemcial composition of humic-like compounds among

405   the cities are somewhat different, as shown by the different AQY peak shapes of this peak, which can be

406   further decomposed by PARAFAC model (Figure S6).

407

408   3.5. Fluorescent Components

409

410   Using the PARAFAC model, we were able to identify six chromophore components (C1–C6) from EEMs

411   (Figure 8 and Table S2). C1 is characterized by a primary peak (Ex/Em) at ~230 nm/375 nm and a

412   secondary peak of ~320 nm/375 nm. C5 also shows two similar peaks, but shifted to a shorter wavelength

413   at Ex (210/280 nm) and Em (373 nm). These two chromophores are characterized as less oxygenated

414   humic-like components (LO-HULIS) (Chen et al., 2016; Chen et al., 2021), with different oxidation

415   states between them, and C5 was likely from primary sources such as coal burning and vehicle emissions,

416   while C1 was secondary production. C2 shows a fluorescence peak (255nm/364 nm) and has been

417   observed in previous studies on fossil burning aerosol but has not been defined (Tang et al., 2020; Chen

418   et al., 2020a). C3, peaking at 240 nm/300 nm (Ex) and 414 nm (Em), is regarded as a highly oxygenated

419   humic-like chromophore (HO-HULIS), commonly considered as a secondary formation (Chen et al.,

420   2016; Yan and Kim, 2017; Cao et al., 2021). In particular, Hawkins et al. (2016) and Aiona et al. (2017)

421   found that the fluorescence generated by the aqueous-phase reaction of aldehydes with ammonium sul-

422   fate or amines highly matched the HULIS fluorescence peak (Ex < 250/~300 nm, Em > 400 nm) in

423   WSOA of ambient aerosol. C4 (Ex = 225/275 nm and Em = 338 nm) and C6 (Ex = 220 nm, Em = 292

424   nm) both peak at a short wavelength and are usually characterized as protein-like fluorophores (PLS)

425   (Yan and Kim, 2017; Wu et al., 2019; Chen et al., 2020a; Chen et al., 2021), but can also be phenol-like

426   substances or other aromatic compounds, especially for urban ambient aerosol samples (Barsotti et al.,

427   2016; Chen et al., 2020a; Cao et al., 2021; Deng et al., 2022). The averaged relative contributions of

428   chromophores are dominated by HULIS chromophores (C1, C3, and C5) with a total contribution of

429   56.5–68.4%, followed by PLS chromophores (C4 and C6) (16.5–22.3%), and then the undefined

430   chromophores (C2) (14.9–20.8%) (Figure 2e). Specifically, there were significant differences in the

431   relative content of each fluorescent component in four cities. For example, the content of C1 was higher

432   in YC (38.4% vs. 28.7–31.0% in the other three cities) (t-test, $P < 0.01$), the contents of C2 and C4 were

433   higher in LZ (20.8% and 21.1%) than in other three cities (14.7–16.2% and 11.2–18.6%) (t-test, $P < 0.01$),

434   and the content of C3 was significantly higher in UR than in YC, XN and LZ (28.6% vs. 18.8–19.4%)

435   (t-test, $P < 0.01$).

436

437   3.6. Source apportionment of WSOA by PMF analysis

438

439   Four WSOA factors were identified through PMF analysis on the high-resolution mass spectra of WSOA

440   at four cities, including a water-soluble primary OA (WS-POA), two highly oxidized oxygenated OA

441   (HO-OOA1 and HO-OOA2), and a less oxidized oxygenated OA (LO-OOA) (Figure 9). The mass spec-

442   trum of WS-POA is dominated by $C_xH_y^+$ (51%) fragment ions, followed by $C_xH_yO_1^+$ (24%), $C_xH_yO_2^+$

443   (14%), $C_xH_yN_p^+$ (6%), H_yO_1 (4%), and $C_xH_yO_zN_p^+$ (1%). The WS-POA has the lowest O/C (0.47) and the

444   highest H/C (1.68) among the four factors, but its O/C is much higher than those of online measurement

445   decomposed POA (<0.1) (Xu et al., 2020a; Zhao et al., 2022). In addition to oxygen-containing ions, the

446   WS-POA presents a few characteristics similar to those of the online measurement decomposed POA,

447   such as relatively high m/z at 55 and 57 with the ratio of m/z 55/57 being 2.67, 60 (fraction of signal =

448   0.39%), and 115 (fraction of signal = 0.21%), which could be related with cooking, biomass burning,

449   and coal combustion, respectively. These results suggest that WS-POA factor in our study represents

450   mixed primary sources. The mass contribution of WS-POA was 26.2 ± 19.1%, 42.9 ± 15.2%, 30.7 ±

451   10.2%, and 48.8 ± 9.3% in YC, XN, UR, and LZ, respectively.

452

453   The mass spectrum of LO-OOA also shows a pronounced signal at m/z 115 (signal fraction = 0.36%)

454   and its concentration is highly correlated with some signals of PAHs, such as $C_6H_3^+$, $C_7H_4^+$, $C_8H_5^+$, and

455    $C_9H_5^+$ (Figure 9), indicating that LO-OOA was associated with coal combustion-induced WSOA. How-

456   ever, LO-OOA has significantly higher OS_c (-0.05 vs. -0.74 for LO-OOA and WS-POA, respectively),

457   lower $C_xH_y^+$ ions (33%), and higher oxygenated ions combined (57% in total), including $C_xH_yO_1^+$ (32%),

458    $C_xH_yO_2^+$ (18%), H_yO_1 (4%), and $C_xH_yO_zN_p^+$ (2%), compared to the primary factor. These imply that LO-

459   OOA may represent a low oxidation OOA associated with coal combustion-induced WSOA. The same

460   factor was also observed in water-soluble aerosol samples from Beijing during winter (Hu et al., 2020).

461   The mass contribution of LO-OOA was 25.2 ± 15.3%, 10.9 ± 3.3%, 6.4 ± 2.3%, and 7.3 ± 1.6% in YC,

462   XN, UR, and LZ, respectively.

463

464   The mass spectrum of HO-OOA1 was characterized by a distinct signal at m/z 44, which accounted for

465   20.4% of the total signal and was mainly composed of CO_2^+ (94%). Additionally, HO-OOA1 exhibited a

466   high O/C value (0.97), indicating its high oxidation. HO-OOA1 was significantly correlated nitrate ($r =$

467   0.33, P < 0.01) and odd oxygen ($O_x = O_3 + NO_2$) which are the products of photochemical processes

468   (Figure S7), suggesting that HO-OOA1 was photochemically produced (Herndon et al., 2008; Ye et al.,

469   2017). The mass contribution of HO-OOA1 were 29.6 ± 18.1%, 37.2 ± 10.1%, 13.4 ± 10.2%, and 38.3

470   ± 8.5% in YC, XN, UR, and LZ, respectively. The HO-OOA2 exhibited comparable O/C with that of

471   HO-OOA1 (0.99 vs. 0.97), but a higher N/C ratio (0.094 vs. 0.041) and a stronger correlation with RH

472   and sulfate than HO-OOA1, suggesting its potential aqueous processing production (Sun et al., 2016;

473   Wang et al., 2021). Furthermore, HO-OOA2 exhibited a significant correlation with $CH_2O_2^+$ ($r = 0.48$, P

474   < 0.01), a typical fragment ion for glyoxal, which could be generated from ring-breaking in the aqueous-

475   phase oxidation of polycyclic aromatic hydrocarbons (Chhabra et al., 2010; Wang et al., 2020). The mass

476   contribution of HO-OOA2 were 19.0 ± 5.8%, 8.9 ± 6.2%, 49.5 ± 7.2%, and 5.1 ± 2.7% in YC, XN,

477   and LZ, respectively. Overall, the WSOA at LZ had the highest contribution of POA than other cites,

478   while UR had the highest contribution of HO-OOA2 and YC had the highest contribution of LO-OOA

479   (Figure 2).

480

481   To further assess the relative light absorption contributions of WSOA from different sources, the four

482   WSOA factors mentioned above were assigned to Abs_{365} using the multiple linear regression model

483   (MLR), as described in the following equation:

484     $Abs_{365} = a \times [WS\text{-}POA] + b \times [LOOA] + c \times [HOOA\text{-}1] + d \times [HOOA\text{-}2]$

485   where [WS-POA], [LOOA], [HOOA-1], and [HOOA-2] are the mass concentrations of WSOA factors;

486   and a, b, c, and d represent regression coefficients (m^2/g), which represents the MAE value for each factor.

487   The reconstructed Abs_{365} fits well with the measured Abs_{365}, and the slope is close to 1 (Figure S8),

488   indicating the effectiveness of the algorithm. The fitted MAE values were higher for WS-POA and LOOA,

489   with values of 1.34 and 1.33 (m^2/g), respectively (Table S4). These values are comparable to those of

490   FF-POA (1.35) and LOOA (1.24) factors previously determined during the winter in Beijing (Wang et

491   al., 2021). The lower MAE of HO-OOA1 (1.10 m^2/g) may be due to photo-bleaching in photochemical

492   process (Browne et al., 2019; Chen et al., 2020b; Zhang et al., 2021b). The lowest MAE value for HO-

493   OOA2 (0.58 m^2/g) suggests a strong photobleaching effect of the aqueous-phase oxidation process (Wang

494   et al., 2021). The average relative contributions of different WSOA factors to light absorption are shown

495   in Figure 9c. WS-POA was the most important WS-BrC in our study, contributing 60%, 51%, 46%, and

496   30% of Abs_{365} in LZ, XN, UR, and YC, respectively. HO-OOA1 also plays an important role in the

497   absorption of WS-BrC, contributing nearly 30% except in UR (only 13%). Although HO-OOA2 has a

498   small MAE value, its high-quality contribution in UR (50%) makes it an important WS-BrC contributor

499   in UR as well (32%), while it was the least contributing factor to Abs_{365}, with only 2–11% in other three

500   cities. LO-OOA were an equally important contributors to Abs_{365} as WS-POA, with a contribution of 31%

501   vs. 30% in YC, while in other cities, the contribution was around 10%.

502

503   3.7. Chemical transformations of chromophores

504

505   The light-absorption capacity of BrC is closely related to atmospheric aging processes and its chemical

506   composition (Lin et al., 2016; Jiang et al., 2022). To understand the relationship between light-absorption

507   properties and chemical processes, several indexes, including O/C, H/C, N/C, and carbon oxidation state

508   (OSc), were investigated for the relationship with MAE$_{365}$ and AAE (Figure 10). The indexes of O/C and

509   OSc, which reflect the degree of atmospheric aging, show lower values at LZ than in other cities (on

510   average, 0.58 in LZ vs. 0.64–0.77 in other cities). A significant positive relationship was observed be-

511   tween O/C and MAE$_{365}$ in LZ ($r = 0.57$), while significant negative relationships were observed in YC

512   and UR ($r = -0.70$ and -0.53). These results suggest that photo-enhancement phenomenon occurred in

513   LZ, while photo-bleaching phenomenon occurred in other three cities. Fitting MAE$_{365}$ vs. O/C for all the

514   data of four cities by least-squares linear regression (Figure S9), the fitting trend turns when O/C is about

515   0.64 (MAE$_{365}$ = 1.04×O/C+0.58, when O/C<0.64; MAE$_{365}$ = –1.23×O/C+1.90, when O/C≥0.64). A sim-

516   ilar phenomenon was found by Jiang et al. (2022) in different polar solvent extracts of Beijing PM$_{2.5}$

517   filter samples, which suggests that chemical processing is dominated by functionalization for low O/C

518   period, while it was mainly dominated by fragmentation for high O/C period. Therefore, we infer that

519   the photo-enhancement phenomenon in LZ probably due to the initial aging of fresh WSOA.

520

521   The variation between MAE$_{365}$ and H/C was broadly opposite to that of O/C. A significant positive cor-

522   relation between MAE$_{365}$ and H/C was observed in YC and UR, suggesting higher MAE$_{365}$ for fresh

523   aerosol. MAE$_{365}$ values showed significantly positive correlation with N/C in YC, XN, and LZ ($r = 0.57$,

524   0.50, 0.51, respectively), while weak correlation in UR ($r = 0.11$), indicating that N-containing organic

525   species are effectively light-absorbing chromophores (Chen et al., 2018). To elucidate the potential chem-

526   ical composition and sources of N-containing species, a correlation analysis between MAE$_{365}$ and 65

527   fitted N-containing fragment ions was conducted. Higher correlation efficiencies were found for C$_x$H$_y$N$_p^+$

528   and C$_x$H$_y$O$_z$N$_p^+$ family ions, such as CHN$^+$, CH$_4$N$^+$, C$_2$H$_3$N$^+$, C$_2$H$_6$N$^+$, C$_3$H$_8$N$^+$, C$_2$HNO$^+$, C$_2$H$_2$NO$^+$,

529   C$_2$H$_5$NO$^+$, and C$_3$H$_4$NO$^+$ (Figure S10). These ions may be associated with amine, imine, N-heterocyclic

530   (e.g. imidazole), organonitrates, and nitroaromatic compounds, which have been proven to be important

531   BrC components in ambient aerosol (Farmer et al., 2010; Sun et al., 2012; Kim et al., 2019;

532   Kasthuriarachchi et al., 2020; Ditto et al., 2022; Jiang et al., 2022).

533

534   The relationship between AAE and O/C was also investigated. Firstly, in YC, AAE increases significantly

535   with increasing O/C (slope= 2.62, $r = 0.55$), which is likely related to highly chemical oxidation and the

536   formation of weakly light-absorbing O-containing functional groups (Sumlin et al., 2017; Zeng et al.,

537   2021), leading to a shift in the absorption spectrum towards UV wavelength (AAE increased) (Zhang et

538   al., 2013; Mo et al., 2018). However, a significant negative relationship between AAE and O/C was

539   observed in LZ (slope = −1.41, r = −0.51). As mentioned above, the initial oxidation occurring in LZ

540   was dominated by functioniztion, which introduces functional groups to form auxochrome or

541   chromophore, leading to absorption enhancement and an absorption spectrum red-shift (AAE decreased)

542   (Lin et al., 2015; Zeng et al., 2021; Jiang et al., 2022). Additionally, the AAE values show a roughly

543   decreasing trend with increasing N/C in the four cities, which maybe due to the increase in the abundance

544   of N-heteroatoms leading to a red shift in the absorption spectrum (Jiang et al., 2022).

545

546   Crossing-correlation among fluorescent chromophores and chemical components of PM$_{2.5}$ were per-

547   formed to infer the possible sources and atmospheric chemical processes of WS-BrC (Figure 11a). The

548   results showed that C1, C3, and C6 are tightly correlated with SNA, especially sulfate, suggesting

549   secondary production sources. Meanwhile, C2, C4, and C5 are tightly correlated with primary species,

550   such as EC, K$^+$, and Cl$^-$, indicating primary emission sources. Furthermore, the fluorescent chromophores

551   were assigned to different WSOA factors based on their correlation. For example, C2, C4, and C5, which

552   are primary sourced chromphores, were significantly correlated with WS-POA. C1, characterized as less

553   oxygenated humic-like components, is significantly correlated with LO-OOA, representing secondary

554   chromophore components with less oxidation. C3, characterized as highly oxygenated humic-like

555   components, is significantly correlated with HO-OOA2, while a significant positive correlation is also

556   observed between C3 and HO-OOA1 when UR data were excluded (Figure S11). Thus C3 was likely

557   produced by aqueous-phase oxidation or photochemical oxidation, with different contributions from

558   these two aging pathways in different cities of our study. C6 showed significant correlation with HO-

559   OOA2, suggesting that this chromophore is a potential aqueous product. Due to the highly overlapping

560   EEM spectra of C6 with phenol chromophores (Barsotti et al., 2016; Chen et al., 2020a) and the signifi-

561   cant correlation between C6 and HO-OOA2, we speculate that C6 may be a phenol-like chromophore

562   and an aqueous-phase oxidation product. Recent studies have shown that benzene and its derivatives,

563   commonly found in coal combustion emission, have also been observed in atmospheric waters such as

564   clouds and fog (Raja et al., 2009). Benzene reacts readily with hydroxyl radicals in aqueous phase (k_{OH}

565   = 4.7×10^5 μM^{-1} min^{-1}), which is much faster than its reaction to other atmospheric radicals such as ozone

21

566   (k_{O_3} = 6.1×10^{-6} μM^{-1} min^{-1}) and nitrate radicals (k_{NO_3} = 4.0×10^{-1} μM^{-1} min^{-1}) or photolysis in the gas phase

567   (Minakata et al., 2009). Thus, it is likely the atmospheric chemistry of benzenes is initiated under •OH

568   at aqueous-phase to form phenol (Borrás and Tortajada-Genaro, 2012; Heath et al., 2013; Faust et al.,

569   2017).

570

571   Combing the information above into a Van Krevelen plot (H:C vs. O:C), which is usually used to describe

572   the evolution of organic aerosols (Heald et al., 2010; Ng et al., 2011; Canagaratna et al., 2015), it is

573   clearly shown that there is a tight relationship between the evolution of chemical processes and the light

574   absorbance of chromaphores. Note that each WSOA factor in the Van Krevelen plot is colored by its

575   fitted MAE$_{365}$ values and sized by the contribution of each WSOA factor to Abs$_{365}$. The six PARAFAC

576   components are associated with different WSOA factors based on their correlation among each other.

577   Specifically, aging processes along the direction of increased OSc from fresh species (WS-POA) to LO-

578   OOA and HO-OOA were clearly observed to be associated with a significant photobleaching

579   phenomenon, as evidenced by a decrease/increase in MAE$_{365}$/AAE values, especially for the aqueous-

580   phase oxidation, which resulted in the lowest MAE$_{365}$ value (0.58 m^2/g) and the highest AAE value (7.18).

581   Therefore, the slope from WS-POA to each OOA components could be used to some extent to describe

582   this photobleching phenomeno, i.e., –0.91 for WS-POA & LO-OOA, –0.53 for WS-POA & HO-OOA1,

583   and –0.34 for WS-POA & HO-OOA2. A lower slope (closer to –1) could be related to the addition of

584   carboxylic acid functional groups, while higher slopes (such as –0.5) could be related with the addition

585   of alcohol/peroxide functional groups. Additionally, the slope for each data set of the sampling sites

586   varied from –1.01 at LZ to –0.89 at XN, –0.78 at UR, and –0.71 at YC, further indicating the different

587   chemcial processes at each site and their different optical properties.

588

589   Figure 11c further shows the EEM profiles of the six PARAFAC components (dashed lines plotted), the

590   locations of the strongest fluorescence peaks (Ex/Em) (circles C1-C6), and the compound categories to

591   which they belong. The possible origins and atmospheric chemical transformations of these chromo-

592   phores are further elucidated by correlating the PMF results. It was found that the division of highly

593   oxygenated species region and less oxygenated species region proposed by Chen et al. (2016) was very

594   consistent with our PMF results, while our results are further subdivided into three regions of fresh spe-

595   cies, less oxidized and highly oxidized species, with each of the three regions circled by different shades

596   of brown boxes in Figure 11c. Note that the chemical transformation of the loss of primary chromophores

597   (fresh species) and the generation of secondary chromophores (less oxidized and highly oxidized species)

598   can occur through either photochemical oxidation or aqueous-phase oxidation, with different contribu-

599   tions from the two aging pathways in different cities. Additionally, some chromophores formed from

600   high oxidation processes have short emission wavelengths, which were originally classified as PLS chro-

601   mophores, providing a reference for determining PLS sources and processes in future studies.

602

603   **4. Conclusions**

604

605   In this study, a comprehensive comparison of the optical properties, potential sources, and chemical pro-

606   cesses of WSOA was conducted using atmospheric aerosols collected from four typical cities in North-

607   west China, namely Yinchuan (YC), Xining (XN), Urumqi (UR), and Lanzhou (LZ). The main conclu-

608   sions and environmental implications are obtained as follows.

609

610   Firstly, the optical properties of WSOA were found to be influenced by its chemical composition. The

611   MAE_{365}, HIX, and BIX values of XN (1.24 m^2/g, 1.29, 1.49) and LZ (1.19 m^2/g, 1.16, 1.52) were higher,

612   lower, and higher than those of YC (1.07 m^2/g, 1.32, 1.48) and UR (0.78 m^2/g, 1.85, 1.28), which prob-

613   ably due to a higher contribution of fresh WSOA in XN and LZ and a higher degree of humification and

614   aging/oxidation of WSOA in YC and UR. Secondly, the optical properties of WSOA were found to be

615   influenced by pH variation. The integrated absorbance (300–450 nm) and MAE_{365} increased monoton-

616   ically with increasing pH in all four cities. The impact of pH on fluorescence EEM was far more complex,

617   involving the rigidity and planarity of molecule structure and the protonating/deprotonating of electron-

618   absorbing (–COOH and –NO$_2$) and electron-donating (–NH$_2$ and –OH) groups connected to the fluoro-

619   phore nuclei. The WSOA in YC and LZ were found to be most sensitive to pH variation and showed

620   different trends, indicating that their chemical structures are rich in different types of acid/base functional

621   groups. Thirdly, the optical properties of WSOA were found to be changed with aging/oxidation pro-

622   cesses. Obvious photo-bleaching were observed in YC and UR, while photo-enhancement was in LZ,

623 reflecting the role of the initial aging (functionalization) and further highly oxidation (fragmentation) of

624 fresh WSOA on the optical properties of WS-BrC based on the analysis of optical properties and bulk

625 chemical characteristics. Finally, the analysis combining chromophores with WSOA factors can be used

626 to illustrate the chemical processes and optical variation by V-K plot and EEMs plot which is useful for

627 understanding the dominated chemical pathway at each city.

628

629 Overall, this study provides insight into the optical properties, sources, and chemical transformations of

630 WS-BrC, which will provide an important reference for future studies to determine the sources and pro-

631 cesses of atmospheric chromophores and further help to estimate the climatic effects of atmospheric

632 aerosols and control carbonaceous aerosol pollution.

633

634

635 **Data availability**

636 The data used in this study can be accessed on request from corresponding author.

637

638 **Author contributions**

639 JX designed the research and MZ, HW, LG and WL collected samples. MZ processed data, plotted the

640 figures, and wrote the manuscript when JX and XZ gave constructive discussion. LZ and WZ had an

641 active role in supporting the experimental work. All authors contributed to the discussions of the results

642 and refinement of the manuscript.

643

644 **Competing interests**

645 The authors declare that they have no conflict of interests.

646

647 **Acknowledgment**

650 **References**

651

652 Aiona, P. K., Lee, H. J., Leslie, R., Lin, P., Laskin, A., Laskin, J., and Nizkorodov, S. A.: Photochemistry

653   of Products of the Aqueous Reaction of Methylglyoxal with Ammonium Sulfate, ACS Earth Sp. Chem.,
654   1, 522-532, https://doi.org/10.1021/acsearthspacechem.7b00075, 2017.

655   Andreae, M. O. and Gelencsér, A.: Black carbon or brown carbon? The nature of light absorbing
656   carbonaceous aerosols, Atmos. Chem. Phys., 6, 3131-3148, https://doi.org/10.5194/acp-6-3131-2006,
657   2006.

658   Barsotti, F., Ghigo, G., and Vione, D.: Computational assessment of the fluorescence emission of phenol
659   oligomers: A possible insight into the fluorescence properties of humic-like substances (HULIS), J.
660   Photochem. Photobiol. A Chem., 315, 87-93, https://doi.org/10.1016/j.jphotochem.2015.09.012, 2016.

661   Baylon, P., Jaffe, D. A., Hall, S. R., Ullmann, K., Alvarado, M. J., and Lefer, B. L.: Impact of Biomass
662   Burning Plumes on Photolysis Rates and Ozone Formation at the Mount Bachelor Observatory, J.
663   Geophys. Res.-Atmos., 123, 2272-2284, https://doi.org/10.1002/2017jd027341, 2018.

664   Birdwell, J. E. and Engel, A. S.: Characterization of dissolved organic matter in cave and spring waters
665   using UV-Vis absorbance and fluorescence spectroscopy, Org. Geochem., 41, 270-280,
666   https://doi.org/10.1016/j.orggeochem.2009.11.002, 2010.

667   Borrás, E. and Tortajada-Genaro, L. A.: Secondary organic aerosol formation from the photo-oxidation
668   of benzene, Atmos. Environ., 47, 154-163, https://doi.org/10.1016/j.atmosenv.2011.11.020, 2012.

669   Bosch, C., Andersson, A., Kirillova, E. N., Budhavant, K., Tiwari, S., Praveen, P. S., Russell, L. M.,
670   Beres, N. D., Ramanathan, V., and Gustafsson, Ö.: Source-diagnostic dual-isotope composition and
671   optical properties of water-soluble organic carbon and elemental carbon in the South Asian outflow
672   intercepted   over   the   Indian   Ocean,   J.   Geophys.   Res.-Atmos.,   119,   11743-11759,
673   https://doi.org/10.1002/2014jd022127, 2014.

674   Browne, E. C., Zhang, X., Franklin, J. P., Ridley, K. J., Kirchstetter, T. W., Wilson, K. R., Cappa, C. D.,
675   and Kroll, J. H.: Effect of heterogeneous oxidative aging on light absorption by biomass burning organic
676   aerosol, Aerosol Sci. Technol., 53, 663-674, https://doi.org/10.1080/02786826.2019.1599321, 2019.

677   Canagaratna, M. R., Jimenez, J. L., Kroll, J. H., Chen, Q., Kessler, S. H., Massoli, P., Hildebrandt Ruiz,
678   L., Fortner, E., Williams, L. R., Wilson, K. R., Surratt, J. D., Donahue, N. M., Jayne, J. T., and Worsnop,
679   D. R.: Elemental ratio measurements of organic compounds using aerosol mass spectrometry:
680   characterization, improved calibration, and implications, Atmos. Chem. Phys., 15, 253-272,
681   https://doi.org/10.5194/acp-15-253-2015, 2015.

682   Cao, T., Li, M., Zou, C., Fan, X., Song, J., Jia, W., Yu, C., Yu, Z., and Peng, P. a.: Chemical composition,
683   optical properties, and oxidative potential of water- and methanol-soluble organic compounds emitted
684   from the combustion of biomass materials and coal, Atmos. Chem. Phys., 21, 13187-13205,
685   https://doi.org/10.5194/acp-21-13187-2021, 2021.

686   Chen, Q., Hua, X., Li, J., Chang, T., and Wang, Y.: Diurnal evolutions and sources of water-soluble
687   chromophoric aerosols over Xi'an during haze event, in Northwest China, Sci. Total Environ., 786,
688   147412, https://doi.org/10.1016/j.scitotenv.2021.147412, 2021.

689   Chen, Q., Li, J., Hua, X., Jiang, X., Mu, Z., Wang, M., Wang, J., Shan, M., Yang, X., Fan, X., Song, J.,
690   Wang, Y., Guan, D., and Du, L.: Identification of species and sources of atmospheric chromophores by
691   fluorescence excitation-emission matrix with parallel factor analysis, Sci. Total Environ., 718, 137322,
692   https://doi.org/10.1016/j.scitotenv.2020.137322, 2020a.

693   Chen, Q., Miyazaki, Y., Kawamura, K., Matsumoto, K., Coburn, S., Volkamer, R., Iwamoto, Y., Kagami,
694   S., Deng, Y., Ogawa, S., Ramasamy, S., Kato, S., Ida, A., Kajii, Y., and Mochida, M.: Characterization
695   of Chromophoric Water-Soluble Organic Matter in Urban, Forest, and Marine Aerosols by HR-ToF-AMS
696   Analysis and Excitation-Emission Matrix Spectroscopy, Environ. Sci. Technol., 50, 10351-10360,
697   https://doi.org/10.1021/acs.est.6b01643, 2016.

698   Chen, W., Westerhoff, P., Leenheer, J. A., and Booksh, K.: Fluorescence excitation-emission matrix
699   regional integration to quantify spectra for dissolved organic matter, Environ. Sci. Technol., 37, 5701-
700   5710, https://doi.org/10.1021/es034354c, 2003.

701   Chen, Y. and Bond, T. C.: Light absorption by organic carbon from wood combustion, Atmos. Chem.
702   Phys., 10, 1773-1787, https://doi.org/10.5194/acp-10-1773-2010, 2010.

703   Chen, Y., Ge, X., Chen, H., Xie, X., Chen, Y., Wang, J., Ye, Z., Bao, M., Zhang, Y., and Chen, M.:
704   Seasonal light absorption properties of water-soluble brown carbon in atmospheric fine particles in
705   Nanjing, China, Atmos. Environ., 187, 230-240, https://doi.org/10.1016/j.atmosenv.2018.06.002, 2018.

706   Chen, Y., Xie, X., Shi, Z., Li, Y., Gai, X., Wang, J., Li, H., Wu, Y., Zhao, X., Chen, M., and Ge, X.: Brown
707   carbon in atmospheric fine particles in Yangzhou, China: Light absorption properties and source
708   apportionment, Atmos. Res., 244, 105028, https://doi.org/10.1016/j.atmosres.2020.105028, 2020b.

709   Cheng, Y., He, K.-b., Du, Z.-y., Engling, G., Liu, J.-m., Ma, Y.-l., Zheng, M., and Weber, R. J.: The
710   characteristics of brown carbon aerosol during winter in Beijing, Atmos. Environ., 127, 355-364,
711   https://doi.org/10.1016/j.atmosenv.2015.12.035, 2016.

712   Chhabra, P. S., Flagan, R. C., and Seinfeld, J. H.: Elemental analysis of chamber organic aerosol using
713   an aerodyne high-resolution aerosol mass spectrometer, Atmos. Chem. Phys., 10, 4111-4131,
714   https://doi.org/10.5194/acp-10-4111-2010, 2010.

715   Chow, J. C., Watson, J. G., Chen, L. W., Chang, M. C., Robinson, N. F., Trimble, D., and Kohl, S.: The
716   IMPROVE_A temperature protocol for thermal/optical carbon analysis: maintaining consistency with a
717   long-term database, J. Air Waste Manag. Assoc., 57, 1014-1023, https://doi.org/10.3155/1047-
718   3289.57.9.1014, 2007.

719   Cox, J. S., Smith, D. S., Warren, L. A., and Ferris, F. G.: Characterizing Heterogeneous Bacterial Surface
720   Functional Groups Using Discrete Affinity Spectra for Proton Binding, Environ. Sci. Technol., 33, 4514-
721   4521, https://doi.org/10.1021/es990627l, 1999.

722   Dao, X., Di, S., Zhang, X., Gao, P., Wang, L., Yan, L., Tang, G., He, L., Krafft, T., and Zhang, F.:
723   Composition and sources of particulate matter in the Beijing-Tianjin-Hebei region and its surrounding
724   areas   during   the   heating   season,   Chemosphere,   291,   132779,
725   https://doi.org/10.1016/j.chemosphere.2021.132779, 2022.

726   Deng, J., Ma, H., Wang, X., Zhong, S., Zhang, Z., Zhu, J., Fan, Y., Hu, W., Wu, L., Li, X., Ren, L.,
727   Pavuluri, C. M., Pan, X., Sun, Y., Wang, Z., Kawamura, K., and Fu, P.: Measurement report: Optical
728   properties and sources of water-soluble brown carbon in Tianjin, North China – insights from organic
729   molecular compositions, Atmos. Chem. Phys., 22, 6449-6470, https://doi.org/10.5194/acp-22-6449-2022,
730   2022.

731   Ditto, J. C., Machesky, J., and Gentner, D. R.: Analysis of reduced and oxidized nitrogen-containing
732   organic compounds at a coastal site in summer and winter, Atmos. Chem. Phys., 22, 3045-3065,

733   https://doi.org/10.5194/acp-22-3045-2022, 2022.

734   Du, Z., He, K., Cheng, Y., Duan, F., Ma, Y., Liu, J., Zhang, X., Zheng, M., and Weber, R.: A yearlong
735   study of water-soluble organic carbon in Beijing II: Light absorption properties, Atmos. Environ., 89,
736   235-241, https://doi.org/10.1016/j.atmosenv.2014.02.022, 2014.

737   Fan, X., Cao, T., Yu, X., Wang, Y., Xiao, X., Li, F., Xie, Y., Ji, W., Song, J., and Peng, P. a.: The
738   evolutionary behavior of chromophoric brown carbon during ozone aging of fine particles from biomass
739   burning, Atmos. Chem. Phys., 20, 4593-4605, https://doi.org/10.5194/acp-20-4593-2020, 2020.

740   Fan, X. J., Wei, S. Y., Zhu, M. B., Song, J. Z., and Peng, P. A.: Comprehensive characterization of humic-
741   like substances in smoke PM2.5 emitted from the combustion of biomass materials and fossil fuels,
742   Atmos. Chem. Phys., 16, 13321-13340, https://doi.org/10.5194/acp-16-13321-2016, 2016.

743   Fan, X. J., Cao, T., Xu-Fang, Y. U., Song, J. Z., Wang, Y., & Xiao, X., et al.: Emission characteristics and
744   optical properties of extractable brown carbon from residential wood combustion, China Environ. Sci.,
745   39, 3215-3224, https://doi.org/10.19674/j.cnki.issn1000-6923.2019.0380, 2019.

746   Farmer, D. K., Matsunaga, A., Docherty, K. S., Surratt, J. D., Seinfeld, J. H., Ziemann, P. J., and Jimenez,
747   J. L.: Response of an aerosol mass spectrometer to organonitrates and organosulfates and implications
748   for atmospheric chemistry, Proc. Natl. Acad. Sci. U. S. A., 107, 6670-6675,
749   https://doi.org/10.1073/pnas.0912340107, 2010.

750   Faust, J. A., Wong, J. P., Lee, A. K., and Abbatt, J. P.: Role of Aerosol Liquid Water in Secondary Organic
751   Aerosol Formation from Volatile Organic Compounds, Environ. Sci. Technol., 51, 1405-1413,
752   https://doi.org/10.1021/acs.est.6b04700, 2017.

753   Fellman, J. B., Hood, E., and Spencer, R. G. M.: Fluorescence spectroscopy opens new windows into
754   dissolved organic matter dynamics in freshwater ecosystems: A review, Limnol. Oceanogr., 55, 2452-
755   2462, https://doi.org/10.4319/lo.2010.55.6.2452, 2010.

756   Fu, P., Kawamura, K., Chen, J., Qin, M., Ren, L., Sun, Y., Wang, Z., Barrie, L. A., Tachibana, E., Ding,
757   A., and Yamashita, Y.: Fluorescent water-soluble organic aerosols in the High Arctic atmosphere, Sci.
758   Rep., 5, 9845, https://doi.org/10.1038/srep09845, 2015.

759   Ge, X., Li, L., Chen, Y., Chen, H., Wu, D., Wang, J., Xie, X., Ge, S., Ye, Z., Xu, J., and Chen, M.: Aerosol
760   characteristics and sources in Yangzhou, China resolved by offline aerosol mass spectrometry and other
761   techniques, Environ. Pollut., 225, 74-85, https://doi.org/10.1016/j.envpol.2017.03.044, 2017.

762   Ghosh, K. and Schnitzer, M.: Fluorescence Excitation-Spectra and Viscosity Behavior of a Fulvic-Acid
763   and Its Copper and Iron Complexes, Soil Sci. Soc. Am. J., 45, 25-29, https://doi.org/
764   10.2136/sssaj1981.03615995004500010005x, 1981.

765   Hawkins, L. N., Lemire, A. N., Galloway, M. M., Corrigan, A. L., Turley, J. J., Espelien, B. M., and De
766   Haan, D. O.: Maillard Chemistry in Clouds and Aqueous Aerosol As a Source of Atmospheric Humic-
767   Like Substances, Environ. Sci. Technol., 50, 7443-7452, https://doi.org/10.1021/acs.est.6b00909, 2016.

768   Heald, C. L., Kroll, J. H., Jimenez, J. L., Docherty, K. S., DeCarlo, P. F., Aiken, A. C., Chen, Q., Martin,
769   S. T., Farmer, D. K., and Artaxo, P.: A simplified description of the evolution of organic aerosol
770   composition in the atmosphere, Geophys. Res. Lett., 37, L08803, https://doi.org/10.1029/2010gl042737,
771   2010.

772   Heath, A. A., Ehrenhauser, F. S., and Valsaraj, K. T.: Effects of temperature, oxygen level, ionic strength,
773   and pH on the reaction of benzene with hydroxyl radicals in aqueous atmospheric systems, J. Environ.
774   Chem. Eng., 1, 822-830, https://doi.org/10.1016/j.jece.2013.07.023, 2013.

775   Hecobian, A., Zhang, X., Zheng, M., Frank, N., Edgerton, E. S., and Weber, R. J.: Water-Soluble Organic
776   Aerosol material and the light-absorption characteristics of aqueous extracts measured over the
777   Southeastern United States, Atmos. Chem. Phys., 10, 5965-5977, https://doi.org/10.5194/acp-10-5965-
778   2010, 2010.

779   Herndon, S. C., Onasch, T. B., Wood, E. C., Kroll, J. H., Canagaratna, M. R., Jayne, J. T., Zavala, M. A.,
780   Knighton, W. B., Mazzoleni, C., Dubey, M. K., Ulbrich, I. M., Jimenez, J. L., Seila, R., de Gouw, J. A.,
781   de Foy, B., Fast, J., Molina, L. T., Kolb, C. E., and Worsnop, D. R.: Correlation of secondary organic
782   aerosol with odd oxygen in Mexico City, Geophys. Res. Lett., 35, https://doi.org/10.1029/2008gl034058,
783   2008.

784   Hu, R., Xu, Q., Wang, S., Hua, Y., Bhattarai, N., Jiang, J., Song, Y., Daellenbach, K. R., Qi, L., Prevot,
785   A. S. H., and Hao, J.: Chemical characteristics and sources of water-soluble organic aerosol in southwest
786   suburb of Beijing, J. Environ. Sci., 95, 99-110, https://doi.org/10.1016/j.jes.2020.04.004, 2020.

787   Huang, R. J., Yang, L., Cao, J., Chen, Y., Chen, Q., Li, Y., Duan, J., Zhu, C., Dai, W., Wang, K., Lin, C.,
788   Ni, H., Corbin, J. C., Wu, Y., Zhang, R., Tie, X., Hoffmann, T., O'Dowd, C., and Dusek, U.: Brown
789   Carbon Aerosol in Urban Xi'an, Northwest China: The Composition and Light Absorption Properties,
790   Environ. Sci. Technol., 52, 6825-6833, https://doi.org/10.1021/acs.est.8b02386, 2018.

791   Huang, R. J., Yang, L., Shen, J., Yuan, W., Gong, Y., Guo, J., Cao, W., Duan, J., Ni, H., Zhu, C., Dai, W.,
792   Li, Y., Chen, Y., Chen, Q., Wu, Y., Zhang, R., Dusek, U., O'Dowd, C., and Hoffmann, T.: Water-Insoluble
793   Organics Dominate Brown Carbon in Wintertime Urban Aerosol of China: Chemical Characteristics and
794   Optical Properties, Environ. Sci. Technol., 54, 7836-7847, https://doi.org/10.1021/acs.est.0c01149, 2020.

795   Huang, R. J., Zhang, Y., Bozzetti, C., Ho, K. F., Cao, J. J., Han, Y., Daellenbach, K. R., Slowik, J. G.,
796   Platt, S. M., Canonaco, F., Zotter, P., Wolf, R., Pieber, S. M., Bruns, E. A., Crippa, M., Ciarelli, G.,
797   Piazzalunga, A., Schwikowski, M., Abbaszade, G., Schnelle-Kreis, J., Zimmermann, R., An, Z., Szidat,
798   S., Baltensperger, U., El Haddad, I., and Prevot, A. S.: High secondary aerosol contribution to particulate
799   pollution during haze events in China, Nature., 514, 218-222, https://doi.org/10.1038/nature13774, 2014.

800   Jiang, X., Liu, D., Li, Q., Tian, P., Wu, Y., Li, S., Hu, K., Ding, S., Bi, K., Li, R., Huang, M., Ding, D.,
801   Chen, Q., Kong, S., Li, W., Pang, Y., and He, D.: Connecting the Light Absorption of Atmospheric
802   Organic Aerosols with Oxidation State and Polarity, Environ. Sci. Technol., 56, 12873-12885,
803   https://doi.org/10.1021/acs.est.2c02202, 2022.

804   Kasthuriarachchi, N. Y., Rivellini, L. H., Chen, X., Li, Y. J., and Lee, A. K. Y.: Effect of Relative
805   Humidity on Secondary Brown Carbon Formation in Aqueous Droplets, Environ. Sci. Technol., 54,
806   13207-13216, https://doi.org/10.1021/acs.est.0c01239, 2020.

807   Kim, H., Collier, S., Ge, X., Xu, J., Sun, Y., Jiang, W., Wang, Y., Herckes, P., and Zhang, Q.: Chemical
808   processing of water-soluble species and formation of secondary organic aerosol in fogs, Atmos. Environ.,
809   200, 158-166, https://doi.org/10.1016/j.atmosenv.2018.11.062, 2019.

810   Kirillova, E. N., Andersson, A., Tiwari, S., Srivastava, A. K., Bisht, D. S., and Gustafsson, Ö.: Water-
811   soluble organic carbon aerosols during a full New Delhi winter: Isotope-based source apportionment and

812   optical properties, J. Geophys. Res.-Atmos., 119, 3476-3485, https://doi.org/10.1002/2013jd020041,
813   2014.

814   Lambe, A. T., Cappa, C. D., Massoli, P., Onasch, T. B., Forestieri, S. D., Martin, A. T., Cummings, M. J.,
815   Croasdale, D. R., Brune, W. H., Worsnop, D. R., and Davidovits, P.: Relationship between oxidation level
816   and optical properties of secondary organic aerosol, Environ. Sci. Technol., 47, 6349-6357,
817   https://doi.org/10.1021/es401043j, 2013.

818   Laskin, A., Laskin, J., and Nizkorodov, S. A.: Chemistry of atmospheric brown carbon, Chem. Rev., 115,
819   4335-4382, https://doi.org/10.1021/cr5006167, 2015.

820   Lawaetz, A. J. and Stedmon, C. A.: Fluorescence intensity calibration using the Raman scatter peak of
821   water, Appl. Spectrosc., 63, 936-940, https://doi.org/10.1366/000370209788964548, 2009.

822   Lee, H. J., Laskin, A., Laskin, J., and Nizkorodov, S. A.: Excitation-emission spectra and fluorescence
823   quantum yields for fresh and aged biogenic secondary organic aerosols, Environ. Sci. Technol., 47, 5763-
824   5770, https://doi.org/10.1021/es400644c, 2013.

825   Lei, L., Zhou, W., Chen, C., He, Y., Li, Z., Sun, J., Tang, X., Fu, P., Wang, Z., and Sun, Y.: Long-term
826   characterization of aerosol chemistry in cold season from 2013 to 2020 in Beijing, China, Environ. Pollut.,
827   268, 115952, https://doi.org/10.1016/j.envpol.2020.115952, 2021.

828   Li, C., He, Q., Hettiyadura, A. P. S., Kafer, U., Shmul, G., Meidan, D., Zimmermann, R., Brown, S. S.,
829   George, C., Laskin, A., and Rudich, Y.: Formation of Secondary Brown Carbon in Biomass Burning
830   Aerosol Proxies through NO3 Radical Reactions, Environ. Sci. Technol., 54, 1395-1405,
831   https://doi.org/10.1021/acs.est.9b05641, 2020a.

832   Li, J., Zhang, Q., Wang, G., Li, J., Wu, C., Liu, L., Wang, J., Jiang, W., Li, L., Ho, K. F., and Cao, J.:
833   Optical properties and molecular compositions of water-soluble and water-insoluble brown carbon (BrC)
834   aerosols in northwest China, Atmos. Chem. Phys., 20, 4889-4904, https://doi.org/10.5194/acp-20-4889-
835   2020, 2020b.

836   Lin, P., Fleming, L. T., Nizkorodov, S. A., Laskin, J., and Laskin, A.: Comprehensive Molecular
837   Characterization of Atmospheric Brown Carbon by High Resolution Mass Spectrometry with
838   Electrospray and Atmospheric Pressure Photoionization, Anal. Chem., 90, 12493-12502,
839   https://doi.org/10.1021/acs.analchem.8b02177, 2018.

840   Lin, P., Bluvshtein, N., Rudich, Y., Nizkorodov, S. A., Laskin, J., and Laskin, A.: Molecular Chemistry
841   of Atmospheric Brown Carbon Inferred from a Nationwide Biomass Burning Event, Environ. Sci.
842   Technol., 51, 11561-11570, https://doi.org/10.1021/acs.est.7b02276, 2017.

843   Lin, P., Liu, J., Shilling, J. E., Kathmann, S. M., Laskin, J., and Laskin, A.: Molecular characterization
844   of brown carbon (BrC) chromophores in secondary organic aerosol generated from photo-oxidation of
845   toluene, Phys. Chem. Chem. Phys., 17, 23312-23325, https://doi.org/10.1039/c5cp02563j, 2015.

846   Lin, P., Aiona, P. K., Li, Y., Shiraiwa, M., Laskin, J., Nizkorodov, S. A., and Laskin, A.: Molecular
847   Characterization of Brown Carbon in Biomass Burning Aerosol Particles, Environ. Sci. Technol., 50,
848   11815-11824, https://doi.org/10.1021/acs.est.6b03024, 2016.

849   Liu, C., Liu, Y., Chen, T., Liu, J., and He, H.: Rate constant and secondary organic aerosol formation
850   from the gas-phase reaction of eugenol with hydroxyl radicals, Atmos. Chem. Phys., 19, 2001-2013,
851   https://doi.org/10.5194/acp-19-2001-2019, 2019.

852   Liu, J. M., Wang, P. F., Zhang, H. L., Du, Z. Y., Zheng, B., Yu, Q. Q., Zheng, G. J., Ma, Y. L., Zheng, M.,
853   Cheng, Y., Zhang, Q., and He, K. B.: Integration of field observation and air quality modeling to
854   characterize   Beijing   aerosol   in   different   seasons,   Chemosphere,   242,   125195,
855   https://doi.org/10.1016/j.chemosphere.2019.125195, 2020.

856   McKnight, D. M., Boyer, E. W., Westerhoff, P. K., Doran, P. T., Kulbe, T., and Andersen, D. T.:
857   Spectrofluorometric characterization of dissolved organic matter for indication of precursor organic
858   material and aromaticity, Limnol. Oceanogr., 46, 38-48, https://doi.org/10.4319/lo.2001.46.1.0038, 2001.

859   Mei, Y., Wang, L., and Wu, F.: Effects of water chemistry and concentrations of dissolved organic matter
860   on its fluorescence characteristics and molecular conformation, Chin. J. Geochem., 28, 413-420,
861   https://doi.org/10.1007/s11631-009-0413-2, 2009.

862   Milne, C. J., Kinniburgh, D. G., and Tipping, E.: Generic NICA-Donnan model parameters for proton
863   binding by humic substances, Environ. Sci. Technol., 35, 2049-2059, https://doi.org/10.1021/es000123j,
864   2001.

865   Minakata, D., Li, K., Westerhoff, P., and Crittenden, J.: Development of a group contribution method to
866   predict aqueous phase hydroxyl radical (HO*) reaction rate constants, Environ. Sci. Technol., 43, 6220-
867   6227, https://doi.org/10.1021/es900956c, 2009.

868   Mo, Y., Li, J., Jiang, B., Su, T., Geng, X., Liu, J., Jiang, H., Shen, C., Ding, P., Zhong, G., Cheng, Z.,
869   Liao, Y., Tian, C., Chen, Y., and Zhang, G.: Sources, compositions, and optical properties of humic-like
870   substances in Beijing during the 2014 APEC summit: Results from dual carbon isotope and Fourier-
871   transform ion cyclotron resonance mass spectrometry analyses, Environ. Pollut., 239, 322-331,
872   https://doi.org/10.1016/j.envpol.2018.04.041, 2018.

873   Moise, T., Flores, J. M., and Rudich, Y.: Optical properties of secondary organic aerosols and their
874   changes by chemical processes, Chem. Rev., 115, 4400-4439, https://doi.org/10.1021/cr5005259, 2015.

875   Mok, J., Krotkov, N. A., Arola, A., Torres, O., Jethva, H., Andrade, M., Labow, G., Eck, T. F., Li, Z.,
876   Dickerson, R. R., Stenchikov, G. L., Osipov, S., and Ren, X.: Impacts of brown carbon from biomass
877   burning on surface UV and ozone photochemistry in the Amazon Basin, Sci. Rep., 6, 36940,
878   https://doi.org/10.1038/srep36940, 2016.

879   Murphy, K. R., Stedmon, C. A., Graeber, D., and Bro, R.: Fluorescence spectroscopy and multi-way
880   techniques. PARAFAC, Anal. Methods, 5, 6557-6566, https://doi.org/10.1039/c3ay41160e, 2013.

881   Ng, N. L., Canagaratna, M. R., Jimenez, J. L., Chhabra, P. S., Seinfeld, J. H., and Worsnop, D. R.:
882   Changes in organic aerosol composition with aging inferred from aerosol mass spectra, Atmos. Chem.
883   Phys., 11, 6465-6474, https://doi.org/10.5194/acp-11-6465-2011, 2011.

884   Ni, H., Huang, R. J., Yao, P., Cosijn, M. M., Kairys, N., Zhong, H., and Dusek, U.: Organic aerosol
885   formation and aging processes in Beijing constrained by size-resolved measurements of radiocarbon and
886   stable isotopic 13C, Environ. Int., 158, 106890, https://doi.org/10.1016/j.envint.2021.106890, 2022.

887   Ni, H., Huang, R. J., Pieber, S. M., Corbin, J. C., Stefenelli, G., Pospisilova, V., Klein, F., Gysel-Beer,
888   M., Yang, L., Baltensperger, U., Haddad, I. E., Slowik, J. G., Cao, J., Prevot, A. S. H., and Dusek, U.:
889   Brown Carbon in Primary and Aged Coal Combustion Emission, Environ. Sci. Technol., 55, 5701-5710,
890   https://doi.org/10.1021/acs.est.0c08084, 2021.

891   Ohno, T.: Fluorescence inner-filtering correction for determining the humification index of dissolved

892   organic matter, Environ. Sci. Technol., 36, 742-746, https://doi.org/10.1021/es0155276, 2002.

893   Phillips, S. M. and Smith, G. D.: Further evidence for charge transfer complexes in brown carbon aerosols
894   from excitation-emission matrix fluorescence spectroscopy, J. Phys. Chem. A, 119, 4545-4551,
895   https://doi.org/10.1021/jp510709e, 2015.

896   Phillips, S. M., Bellcross, A. D., and Smith, G. D.: Light Absorption by Brown Carbon in the
897   Southeastern United States is pH-dependent, Environ. Sci. Technol., 51, 6782-6790,
898   https://doi.org/10.1021/acs.est.7b01116, 2017.

899   Psichoudaki, M. and Pandis, S. N.: Atmospheric Aerosol Water-Soluble Organic Carbon Measurement:
900   A Theoretical Analysis, Environ. Sci. Technol., 47, 9791-9798, https://doi.org/10.1021/es402270y, 2013.

901   Qin, J., Zhang, L., Qin, Y., Shi, S., Li, J., Gao, Y., Tan, J., and Wang, X.: pH-Dependent Chemical
902   Transformations of Humic-Like Substances and Further Cognitions Revealed by Optical Methods,
903   Environ. Sci. Technol., https://doi.org/10.1021/acs.est.1c07729, 2022a.

904   Qin, J., Zhang, L., Zhou, X., Duan, J., Mu, S., Xiao, K., Hu, J., and Tan, J.: Fluorescence fingerprinting
905   properties for exploring water-soluble organic compounds in PM2.5 in an industrial city of northwest
906   China, Atmos. Environ., 184, 203-211, https://doi.org/10.1016/j.atmosenv.2018.04.049, 2018.

907   Qin, J., Tan, J., Zhou, X., Yang, Y., Qin, Y., Wang, X., Shi, S., Xiao, K., and Wang, X.: Measurement
908   report: Particle-size-dependent fluorescence properties of water-soluble organic compounds (WSOCs)
909   and their atmospheric implications for the aging of WSOCs, Atmos. Chem. Phys., 22, 465-479,
910   https://doi.org/10.5194/acp-22-465-2022, 2022b.

911   Qin, Y., Yang, Y., Qin, J., Zhang, L., Guo, S., Zhou, X., Chen, R., Tan, J., Xiao, K., and Wang, X.: pH-
912   Responsive Fluorescence EEM to Titrate the Interaction between Fluorophores and Acid/Base Groups in
913   Water-Soluble Organic Compounds of PM2.5, Environ. Sci. Technol. Lett., 8, 108-113,
914   https://doi.org/10.1021/acs.estlett.0c00645, 2020.

915   Raja, S., Raghunathan, R., Kommalapati, R. R., Shen, X., Collett, J. L., and Valsaraj, K. T.: Organic
916   composition of fogwater in the Texas–Louisiana gulf coast corridor, Atmos. Environ., 43, 4214-4222,
917   https://doi.org/10.1016/j.atmosenv.2009.05.029, 2009.

918   Saleh, R.: From Measurements to Models: Toward Accurate Representation of Brown Carbon in Climate
919   Calculations, Curr. Pollut. Rep., 6, 90-104, https://doi.org/10.1007/s40726-020-00139-3, 2020.

920   Shan, Y., Guan, D., Hubacek, K., Zheng, B., Davis, S. J., Jia, L., Liu, J., Liu, Z., Fromer, N., Mi, Z.,
921   Meng, J., Deng, X., Li, Y., Lin, J., Schroeder, H., Weisz, H., and Schellnhuber, H. J.: City-level climate
922   change mitigation in China, Sci. Adv., 4, eaaq0390, https://doi.org/10.1126/sciadv.aaq0390, 2018.

923   Song, C., Gyawali, M., Zaveri, R. A., Shilling, J. E., and Arnott, W. P.: Light absorption by secondary
924   organic aerosol from α-pinene: Effects of oxidants, seed aerosol acidity, and relative humidity, J. Geophys.
925   Res.-Atmos., 118, 11741–711749, https://doi.org/10.1002/jgrd.50767, 2013.

926   Sumlin, B. J., Pandey, A., Walker, M. J., Pattison, R. S., Williams, B. J., and Chakrabarty, R. K.:
927   Atmospheric Photooxidation Diminishes Light Absorption by Primary Brown Carbon Aerosol from
928   Biomass Burning, Environ. Sci. Technol. Lett., 4, 540-545, https://doi.org/10.1021/acs.estlett.7b00393,
929   2017.

930   Sun, W., Huo, J., Li, R., Wang, D., Yao, L., Fu, Q., and Feng, J.: Effects of energy structure differences

931   on chemical compositions and respiratory health of PM2.5 during late autumn and winter in China, Sci.
932   Total Environ., 824, 153850, https://doi.org/10.1016/j.scitotenv.2022.153850, 2022.

933   Sun, Y., Wang, Z., Fu, P., Jiang, Q., Yang, T., Li, J., and Ge, X.: The impact of relative humidity on
934   aerosol composition and evolution processes during wintertime in Beijing, China, Atmos. Environ., 77,
935   927-934, https://doi.org/10.1016/j.atmosenv.2013.06.019, 2013.

936   Sun, Y. L., Zhang, Q., Schwab, J. J., Yang, T., Ng, N. L., and Demerjian, K. L.: Factor analysis of
937   combined organic and inorganic aerosol mass spectra from high resolution aerosol mass spectrometer
938   measurements, Atmos. Chem. Phys., 12, 8537-8551, https://doi.org/10.5194/acp-12-8537-2012, 2012.

939   Sun, Y. L., Du, W., Fu, P. Q., Wang, Q. Q., Li, J., Ge, X. L., Zhang, Q., Zhu, C. M., Ren, L. J., Xu, W.
940   Q., Zhao, J., Han, T. T., Worsnop, D. R., and Wang, Z. F.: Primary and secondary aerosols in Beijing in
941   winter: sources,   variations   and   processes,   Atmos.   Chem.   Phys.,   16,   8309-8329,
942   https://doi.org/10.5194/acp-16-8309-2016, 2016.

943   Sun, Y. L., He, Y., Kuang, Y., Xu, W. Y., Song, S. J., Ma, N., Tao, J. C., Cheng, P., Wu, C., Su, H., Cheng,
944   Y. F., Xie, C. H., Chen, C., Lei, L., Qiu, Y. M., Fu, P. Q., Croteau, P., and Worsnop, D. R.: Chemical
945   Differences Between PM1 and PM2.5 in Highly Polluted Environment and Implications in Air Pollution
946   Studies, Geophys. Res. Lett., 47, e2019GL086288, https://doi.org/10.1029/2019GL086288, 2020.

947   Tan, J., Xiang, P., Zhou, X., Duan, J., Ma, Y., He, K., Cheng, Y., Yu, J., and Querol, X.: Chemical
948   characterization of humic-like substances (HULIS) in PM2.5 in Lanzhou, China, Sci. Total Environ., 573,
949   1481-1490, https://doi.org/10.1016/j.scitotenv.2016.08.025, 2016.

950   Tang, J., Li, J., Su, T., Han, Y., Mo, Y., Jiang, H., Cui, M., Jiang, B., Chen, Y., Tang, J., Song, J., Peng, P.
951   a., and Zhang, G.: Molecular compositions and optical properties of dissolved brown carbon in biomass
952   burning, coal combustion, and vehicle emission aerosols illuminated by excitation–emission matrix
953   spectroscopy and Fourier transform ion cyclotron resonance mass spectrometry analysis, Atmos. Chem.
954   Phys., 20, 2513-2532, https://doi.org/10.5194/acp-20-2513-2020, 2020.

955   Tao, J., Zhang, Z., Zhang, L., Li, J., Wu, Y., Pei, C., and Nie, F.: Quantifying the relative contributions
956   of aqueous phase and photochemical processes to water-soluble organic carbon formation in winter in a
957   megacity   of   South   China,   Chemosphere,   300,   134598,
958   https://doi.org/10.1016/j.chemosphere.2022.134598, 2022.

959   Vidovic, K., Lasic Jurkovic, D., Sala, M., Kroflic, A., and Grgic, I.: Nighttime Aqueous-Phase Formation
960   of Nitrocatechols in the Atmospheric Condensed Phase, Environ. Sci. Technol., 52, 9722-9730,
961   https://doi.org/10.1021/acs.est.8b01161, 2018.

962   Vidović, K., Kroflič, A., Šala, M., and Grgić, I.: Aqueous-Phase Brown Carbon Formation from Aromatic
963   Precursors under Sunlight Conditions, Atmosphere, 11, 131, https://doi.org/10.3390/atmos11020131,
964   2020.

965   Wang, J., Ye, J., Zhang, Q., Zhao, J., Wu, Y., Li, J., Liu, D., Li, W., Zhang, Y., Wu, C., Xie, C., Qin, Y.,
966   Lei, Y., Huang, X., Guo, J., Liu, P., Fu, P., Li, Y., Lee, H. C., Choi, H., Zhang, J., Liao, H., Chen, M., Sun,
967   Y., Ge, X., Martin, S. T., and Jacob, D. J.: Aqueous production of secondary organic aerosol from fossil-
968   fuel emissions in winter Beijing haze, Proc. Natl. Acad. Sci. U. S. A., 118, e2022179118,
969   https://doi.org/10.1073/pnas.2022179118, 2021.

970   Wang, S., Newland, M. J., Deng, W., Rickard, A. R., Hamilton, J. F., Munoz, A., Rodenas, M., Vazquez,

M. M., Wang, L., and Wang, X.: Aromatic Photo-oxidation, A New Source of Atmospheric Acidity, Environ. Sci. Technol., 54, 7798-7806, https://doi.org/10.1021/acs.est.0c00526, 2020.

Wang, X., Heald, C. L., Liu, J., Weber, R. J., Campuzano-Jost, P., Jimenez, J. L., Schwarz, J. P., and Perring, A. E.: Exploring the observational constraints on the simulation of brown carbon, Atmos. Chem. Phys., 18, 635-653, https://doi.org/10.5194/acp-18-635-2018, 2018.

Wang, Y., Hu, M., Lin, P., Tan, T., Li, M., Xu, N., Zheng, J., Du, Z., Qin, Y., Wu, Y., Lu, S., Song, Y., Wu, Z., Guo, S., Zeng, L., Huang, X., and He, L.: Enhancement in Particulate Organic Nitrogen and Light Absorption of Humic-Like Substances over Tibetan Plateau Due to Long-Range Transported Biomass Burning Emissions, Environ. Sci. Technol., 53, 14222-14232, https://doi.org/10.1021/acs.est.9b06152, 2019.

Washenfelder, R. A., Attwood, A. R., Brock, C. A., Guo, H., Xu, L., Weber, R. J., Ng, N. L., Allen, H. M., Ayres, B. R., Baumann, K., Cohen, R. C., Draper, D. C., Duffey, K. C., Edgerton, E., Fry, J. L., Hu, W. W., Jimenez, J. L., Palm, B. B., Romer, P., Stone, E. A., Wooldridge, P. J., and Brown, S. S.: Biomass burning dominates brown carbon absorption in the rural southeastern United States, Geophys. Res. Lett., 42, 653-664, https://doi.org/10.1002/2014gl062444, 2015.

Wen, H., Zhou, Y., Xu, X., Wang, T., Chen, Q., Chen, Q., Li, W., Wang, Z., Huang, Z., Zhou, T., Shi, J., Bi, J., Ji, M., and Wang, X.: Water-soluble brown carbon in atmospheric aerosols along the transport pathway of Asian dust: Optical properties, chemical compositions, and potential sources, Sci. Total Environ., 789, 147971, https://doi.org/10.1016/j.scitotenv.2021.147971, 2021.

Wu, G., Ram, K., Fu, P., Wang, W., Zhang, Y., Liu, X., Stone, E. A., Pradhan, B. B., Dangol, P. M., Panday, A. K., Wan, X., Bai, Z., Kang, S., Zhang, Q., and Cong, Z.: Water-Soluble Brown Carbon in Atmospheric Aerosols from Godavari (Nepal), a Regional Representative of South Asia, Environ. Sci. Technol., 53, 3471-3479, https://doi.org/10.1021/acs.est.9b00596, 2019.

Xie, X., Chen, Y., Nie, D., Liu, Y., Liu, Y., Lei, R., Zhao, X., Li, H., and Ge, X.: Light-absorbing and fluorescent properties of atmospheric brown carbon: A case study in Nanjing, China, Chemosphere, 251, 126350, https://doi.org/10.1016/j.chemosphere.2020.126350, 2020.

Xu, J., Ge, X., Zhang, X., Zhao, W., Zhang, R., and Zhang, Y.: COVID-19 Impact on the Concentration and Composition of Submicron Particulate Matter in a Typical City of Northwest China, Geophys. Res. Lett., 47, e2020GL089035, https://doi.org/10.1029/2020GL089035, 2020a.

Xu, J., Hettiyadura, A. P. S., Liu, Y., Zhang, X., Kang, S., and Laskin, A.: Regional Differences of Chemical Composition and Optical Properties of Aerosols in the Tibetan Plateau, J. Geophys. Res.-Atmos., 125, e2019JD031226, https://doi.org/10.1029/2019jd031226, 2020b.

Xu, J., Hettiyadura, A. P. S., Liu, Y., Zhang, X., Kang, S., and Laskin, A.: Atmospheric Brown Carbon on the Tibetan Plateau: Regional Differences in Chemical Composition and Light Absorption Properties, Environ. Sci. Technol. Lett., 9, 219-225, https://doi.org/10.1021/acs.estlett.2c00016, 2022.

Xu, J., Zhang, Q., Li, X., Ge, X., Xiao, C., Ren, J., and Qin, D.: Dissolved organic matter and inorganic ions in a central Himalayan glacier--insights into chemical composition and atmospheric sources, Environ. Sci. Technol., 47, 6181-6188, https://doi.org/10.1021/es4009882, 2013.

Xu, J. Z., Zhang, Q., Wang, Z. B., Yu, G. M., Ge, X. L., and Qin, X.: Chemical composition and size distribution of summertime $PM_{2.5}$ at a high altitude remote location in the

1011 northeast of the Qinghai–Xizang (Tibet) Plateau: insights into aerosol sources and processing in free
1012 troposphere, Atmos. Chem. Phys., 15, 5069-5081, https://doi.org/10.5194/acp-15-5069-2015, 2015.

1013 Yan, C., Zheng, M., Sullivan, A. P., Bosch, C., Desyaterik, Y., Andersson, A., Li, X., Guo, X., Zhou, T.,
1014 Gustafsson, Ö., and Collett, J. L.: Chemical characteristics and light-absorbing property of water-soluble
1015 organic carbon in Beijing: Biomass burning contributions, Atmos. Environ., 121, 4-12,
1016 https://doi.org/10.1016/j.atmosenv.2015.05.005, 2015.

1017 Yan, G. and Kim, G.: Speciation and Sources of Brown Carbon in Precipitation at Seoul, Korea: Insights
1018 from Excitation-Emission Matrix Spectroscopy and Carbon Isotopic Analysis, Environ. Sci. Technol.,
1019 51, 11580-11587, https://doi.org/10.1021/acs.est.7b02892, 2017.

1020 Yang, H., Xu, G., Mao, H., and Wang, Y.: Spatiotemporal Variation in Precipitation and Water Vapor
1021 Transport Over Central Asia in Winter and Summer Under Global Warming, Front. Earth Sci., 8, 297,
1022 https://doi.org/10.3389/feart.2020.00297, 2020a.

1023 Yang, Y., Qin, J., Qi, T., Zhou, X., Chen, R., Tan, J., Xiao, K., Ji, D., He, K., and Chen, X.: Fluorescence
1024 characteristics of particulate water-soluble organic compounds emitted from coal-fired boilers, Atmos.
1025 Environ., 223, https://doi.org/10.1016/j.atmosenv.2020.117297, 2020b.

1026 Ye, Z., Liu, J., Gu, A., Feng, F., Liu, Y., Bi, C., Xu, J., Li, L., Chen, H., Chen, Y., Dai, L., Zhou, Q., and
1027 Ge, X.: Chemical characterization of fine particulate matter in Changzhou, China, and source
1028 apportionment with offline aerosol mass spectrometry, Atmos. Chem. Phys., 17, 2573-2592,
1029 https://doi.org/10.5194/acp-17-2573-2017, 2017.

1030 Yuan, W., Huang, R.-J., Yang, L., Guo, J., Chen, Z., Duan, J., Wang, T., Ni, H., Han, Y., Li, Y., Chen, Q.,
1031 Chen, Y., Hoffmann, T., and O'Dowd, C.: Characterization of the light-absorbing properties,
1032 chromophore composition and sources of brown carbon aerosol in Xi'an, northwestern China, Atmos.
1033 Chem. Phys., 20, 5129-5144, https://doi.org/10.5194/acp-20-5129-2020, 2020.

1034 Yue, S., Ren, L., Song, T., Li, L., Xie, Q., Li, W., Kang, M., Zhao, W., Wei, L., Ren, H., Sun, Y., Wang,
1035 Z., Ellam, R. M., Liu, C. Q., Kawamura, K., and Fu, P.: Abundance and Diurnal Trends of Fluorescent
1036 Bioaerosols in the Troposphere over Mt. Tai, China, in Spring, J. Geophys. Res.-Atmos., 124, 4158-4173,
1037 https://doi.org/10.1029/2018jd029486, 2019.

1038 Zeng, L., Zhang, A., Wang, Y., Wagner, N. L., Katich, J. M., Schwarz, J. P., Schill, G. P., Brock, C., Froyd,
1039 K. D., Murphy, D. M., Williamson, C. J., Kupc, A., Scheuer, E., Dibb, J., and Weber, R. J.: Global
1040 Measurements of Brown Carbon and Estimated Direct Radiative Effects, Geophys. Res. Lett., 47,
1041 e2020GL088747, https://doi.org/10.1029/2020GL088747, 2020.

1042 Zeng, Y. L., Ning, Y. L., Shen, Z. X., Zhang, L. M., Zhang, T., Lei, Y. L., Zhang, Q., Li, G. H., Xu, H.
1043 M., Ho, S. S. H., and Cao, J. J.: The Roles of N, S, and O in Molecular Absorption Features of Brown
1044 Carbon in PM2.5 in a Typical Semi-Arid Megacity in Northwestern China, J. Geophys. Res.-Atmos.,
1045 126, e2021JD034791, https://doi.org/10.1029/2021jd034791, 2021.

1046 Zhang, X., Lin, Y. H., Surratt, J. D., and Weber, R. J.: Sources, composition and absorption Angstrom
1047 exponent of light-absorbing organic components in aerosol extracts from the Los Angeles Basin, Environ.
1048 Sci. Technol., 47, 3685-3693, https://doi.org/10.1021/es305047b, 2013.

1049 Zhang, X., Ding, X., Talifu, D., Wang, X., Abulizi, A., Maihemuti, M., and Rekefu, S.: Humidity and
1050 PM2.5 composition determine atmospheric light extinction in the arid region of northwest China, J.

Environ. Sci., 100, 279-286, https://doi.org/10.1016/j.jes.2020.07.007, 2021a.

Zhang, X., Xu, J., Kang, S., Sun, J., Shi, J., Gong, C., Sun, X., Du, H., Ge, X., and Zhang, Q.: Regional Differences in the Light Absorption Properties of Fine Particulate Matter Over the Tibetan Plateau: Insights From HR-ToF-AMS and Aethalometer Measurements, J. Geophys. Res.-Atmos., 126, e2021JD035562, https://doi.org/10.1029/2021jd035562, 2021b.

Zhang, Y.-L., El-Haddad, I., Huang, R.-J., Ho, K.-F., Cao, J.-J., Han, Y., Zotter, P., Bozzetti, C., Daellenbach, K. R., Slowik, J. G., Salazar, G., Prévôt, A. S. H., and Szidat, S.: Large contribution of fossil fuel derived secondary organic carbon to water soluble organic aerosols in winter haze in China, Atmos. Chem. Phys., 18, 4005-4017, https://doi.org/10.5194/acp-18-4005-2018, 2018.

Zhang, Y., Schauer, J. J., Zhang, Y., Zeng, L., Wei, Y., Liu, Y., and Shao, M.: Characteristics of particulate carbon emissions from real-world Chinese coal combustion, Environ. Sci. Technol., 42, 5068-5073, https://doi.org/10.1021/es7022576, 2008.

Zhang, Y., Xu, J., Shi, J., Xie, C., Ge, X., Wang, J., Kang, S., and Zhang, Q.: Light absorption by water-soluble organic carbon in atmospheric fine particles in the central Tibetan Plateau, Environ. Sci. Pollut. Res. Int., 24, 21386-21397, https://doi.org/10.1007/s11356-017-9688-8, 2017.

Zhang, Y., Shi, Z., Wang, Y., Liu, L., Zhang, J., Li, J., Xia, Y., Ding, X., Liu, D., Kong, S., Niu, H., Fu, P., Zhang, X., and Li, W.: Fine particles from village air in northern China in winter: Large contribution of primary organic aerosols from residential solid fuel burning, Environ. Pollut., 272, 116420, https://doi.org/10.1016/j.envpol.2020.116420, 2021c.

Zhao, R., Lee, A. K. Y., Huang, L., Li, X., Yang, F., and Abbatt, J. P. D.: Photochemical processing of aqueous atmospheric brown carbon, Atmos. Chem. Phys., 15, 6087-6100, https://doi.org/10.5194/acp-15-6087-2015, 2015.

Zhao, W., Zhang, X., Zhai, L., Shen, X., and Xu, J.: Chemical characterization and sources of submicron aerosols in Lhasa on the Qinghai-Tibet Plateau: Insights from high-resolution mass spectrometry, Sci. Total Environ., 815, 152866, https://doi.org/10.1016/j.scitotenv.2021.152866, 2022.

Zhou, Y., West, C. P., Hettiyadura, A. P. S., Niu, X., Wen, H., Cui, J., Shi, T., Pu, W., Wang, X., and Laskin, A.: Measurement report: Molecular composition, optical properties, and radiative effects of water-soluble organic carbon in snowpack samples from northern Xinjiang, China, Atmos. Chem. Phys., 21, 8531-8555, https://doi.org/10.5194/acp-21-8531-2021, 2021.

Zsolnay, A., Baigar, E., Jimenez, M., Steinweg, B., and Saccomandi, F.: Differentiating with fluorescence spectroscopy the sources of dissolved organic matter in soils subjected to drying, Chemosphere, 38, 45-50, https://doi.org/10.1016/s0045-6535(98)00166-0, 1999.
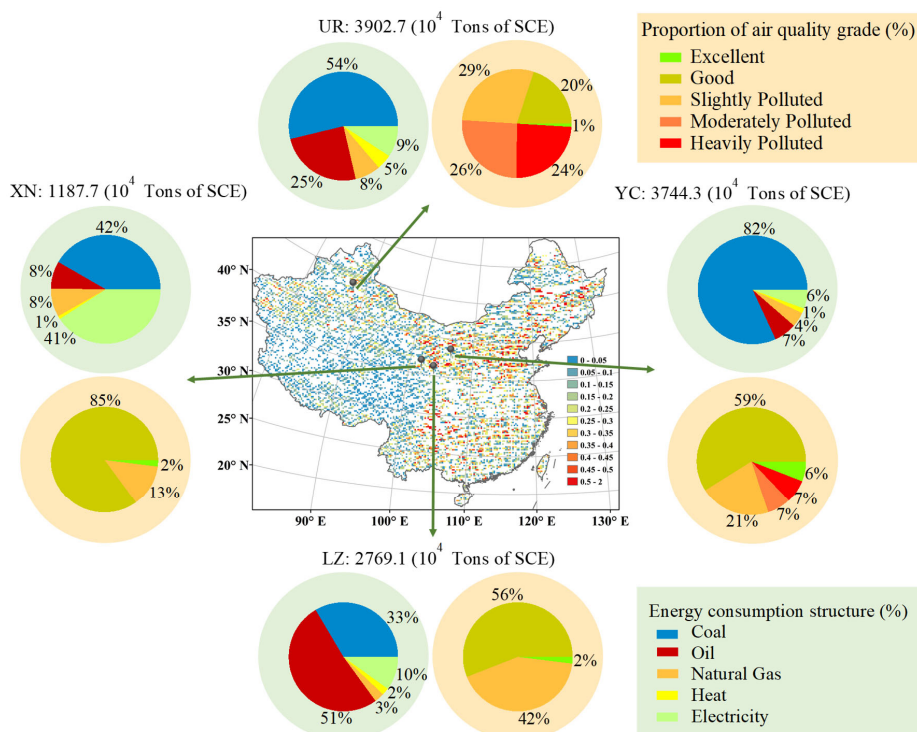
1084
1085   Figure 1. Location map for the sampling sites in this study, and the corresponding energy structure and
1086   air quality in each city during 2019. The spatial variation of SO_2 concentration in China is also shown at
1087   a resolution of 0.25°*0.25° retrieved from OMI satellite data during the sampling period of 2019/12-
1088   2020/1 (http://www.satdatafresh.com/). The mapping tool used was ArcGIS software. Pie charts around
1089   the map show the energy consumption structure during 2019 (left) (source: China Energy Statisti-
1090   cal Yearbook) and the proportion of urban air quality grades during the sampling period (right)
1091   (https://www.zq12369.com/) at each city.
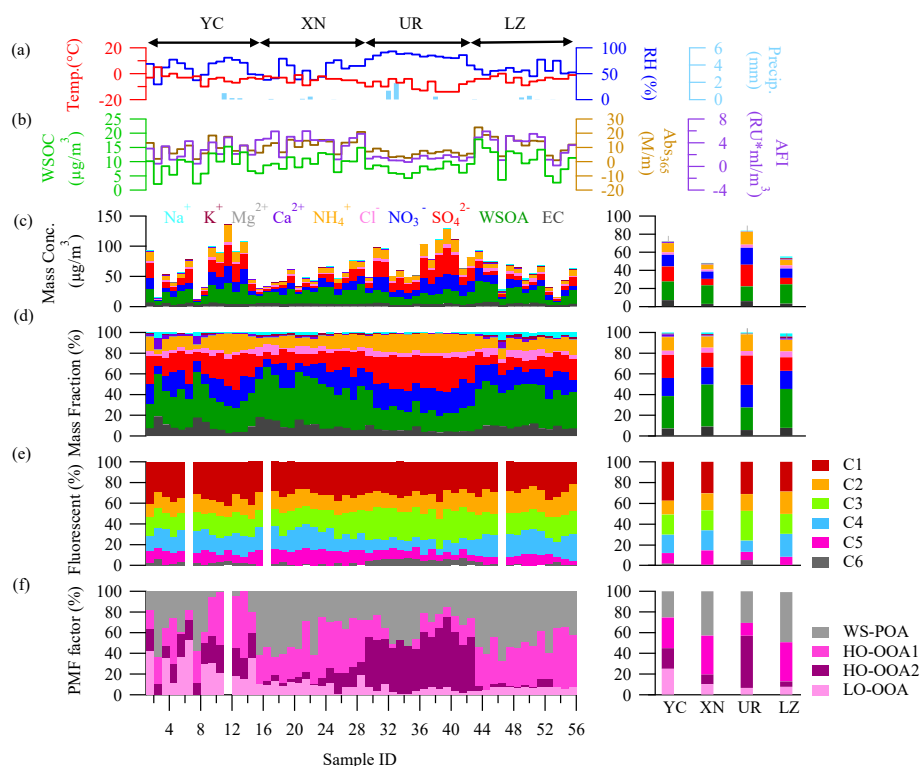
Figure 2. The combo plot for the results of aerosol samples versus sample IDs in this study. (a) Meteorological condition during the sampling including air temperature, relative humidity, and precipitation; (b) WSOC concentrations, the light-absorption (Abs), and average fluorescence intensity (AFI) of WSOA; (c) the concentrations of total identified species (WSIs, OM, and EC); (d) The relative abundance of total identified species; (e) The relative abundances of the identified six fluorescent components by PARAFAC analysis; (f) Mass contributions of the factors resolved by PMF analysis on WSOA.
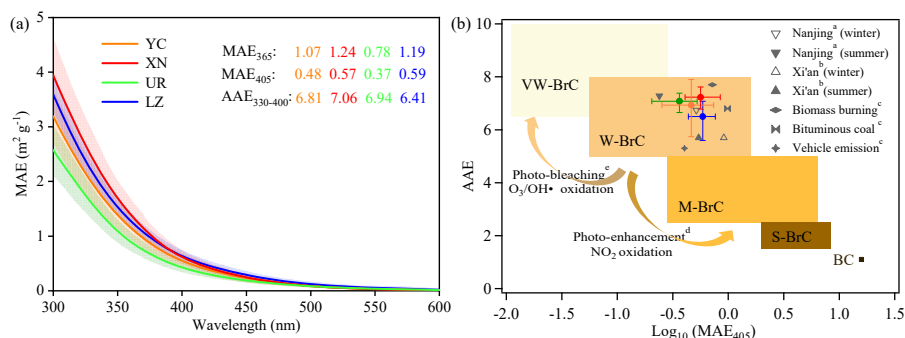
Figure 3. (a) The average MAE spectrum and their standard deviations of WS-BrC in each city represented by different colors. (b) Graphical representation of the optical-based BrC classes in the $\log_{10}(MAE_{405})$-AAE space (Saleh, 2020). The shaded areas respectively indicate very weakly (VW),

1104   weakly (W), moderately (M), and strongly (S) absorbing BrC and absorbing BC. Grey marks indi-
1105   cate the data from previous studies about ambient BrC aerosol, i.e., [a](Chen et al., 2018) [b](Huang et
1106   al., 2018) [c](Tang et al., 2020). The curve with the arrowhead displays the variation tendency of
1107   optical properties of the lab-generated BrC aerosol and aged in the presence of NO_3 or O_3/OH rad-
1108   icals, i.e., [d](Li et al., 2020a) [e](Browne et al., 2019).

1109
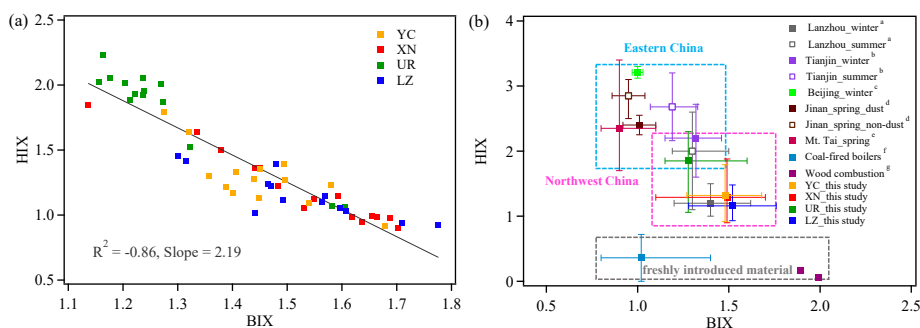
1110

1111   Figure 4. (a) Scatter plots of the humification index (HIX) as a function of the biological index (BIX)
1112   for WSOA in four cities. (b) Comparison plot of HIX versus BIX for this study and previous litera-
1113   tures, including WSOA from ambient aerosols in Lanzhou [a](Qin et al., 2018), Tianjin [b](Deng et al.,
1114   2022), Beijing [c](Qin et al., 2022b), Jinan [d](Wen et al., 2021), Mt. Tai [e](Yue et al., 2019), and from
1115   coal-fired aerosols [f](Yang et al., 2020b), and biomass burning aerosols [g](Fan, 2019).

1116
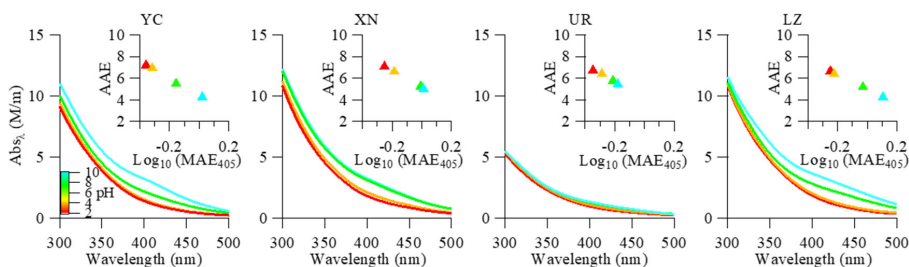
1117

1118   Figure 5. The Influence of pH on absorbance spectra (the insert figure shows the $\log_{10}(MAE_{405})$-
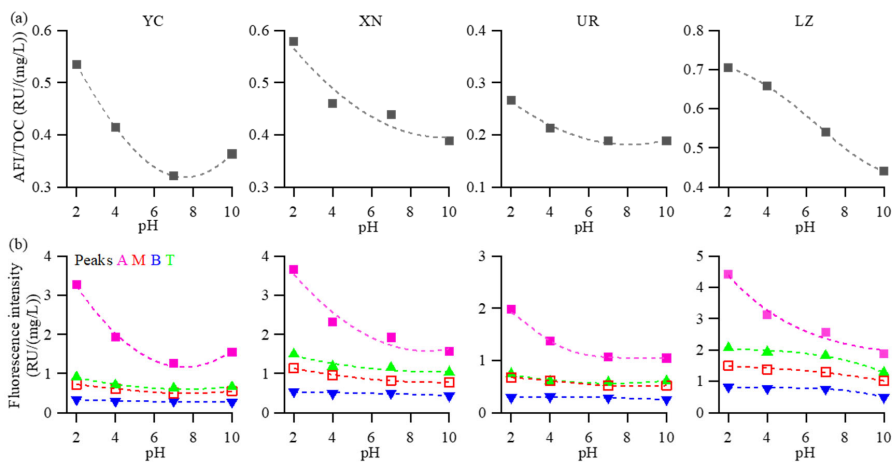1119   AAE values at different pH).
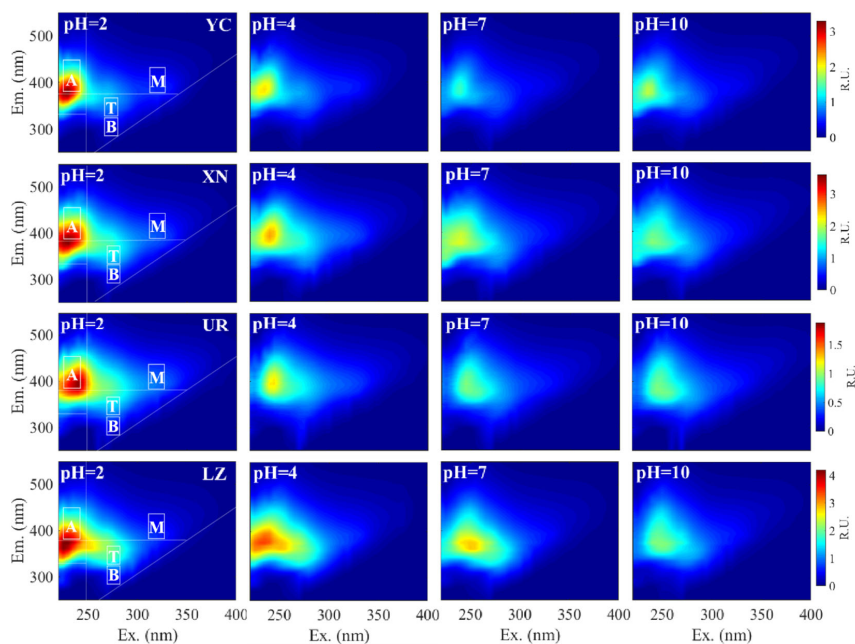
Figure 6. EEMs of WSOA at different pH values.
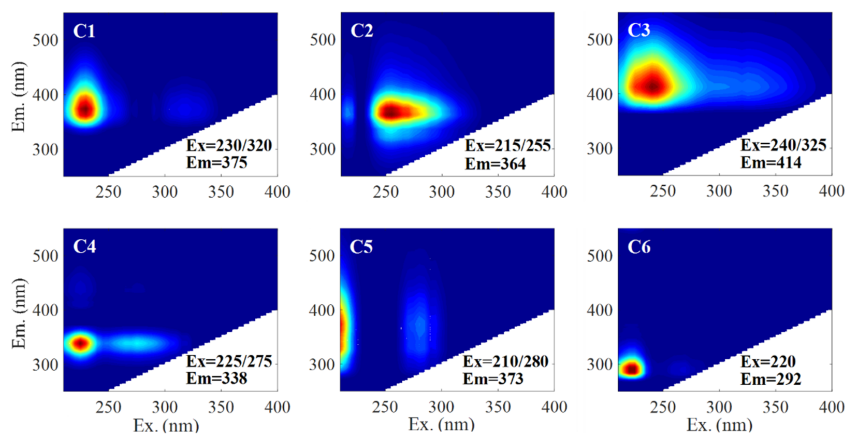

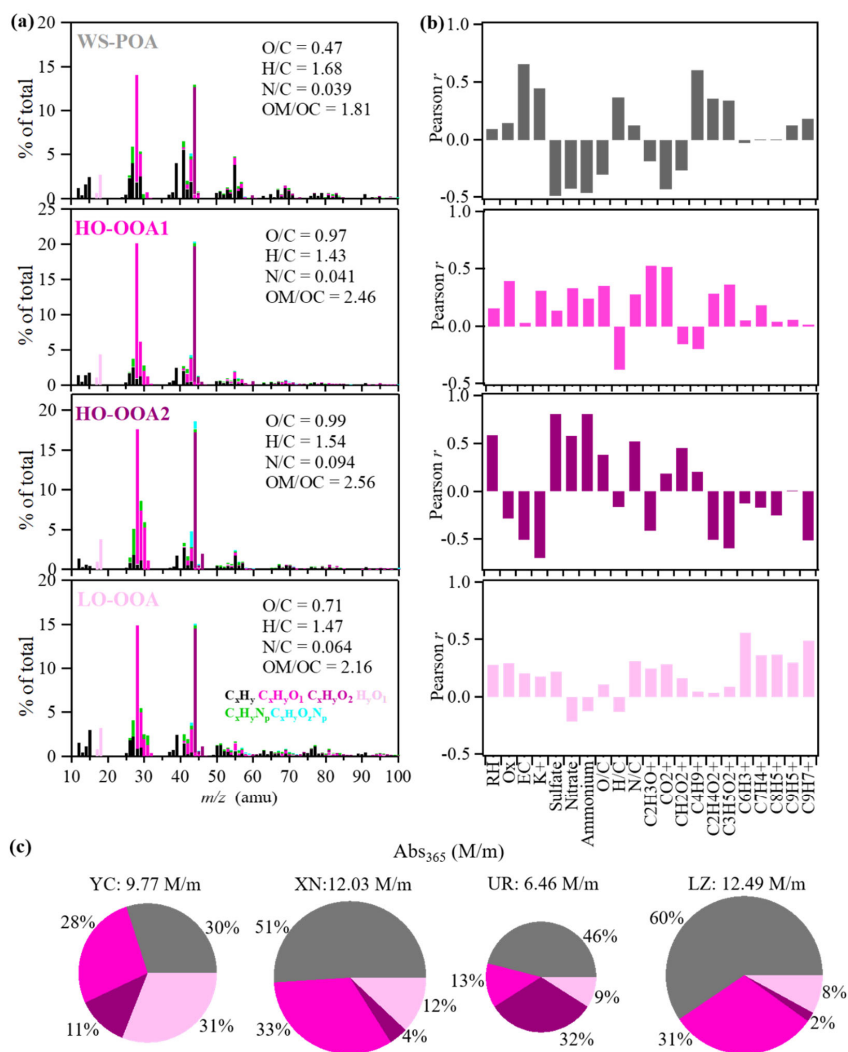Figure 7. (a) The AFI/TOC and (b) maximum peak intensity of major fluorescence peaks as a function of pH values.

Figure 8. The EEM components identified by the PARAFAC model for the WSOA.

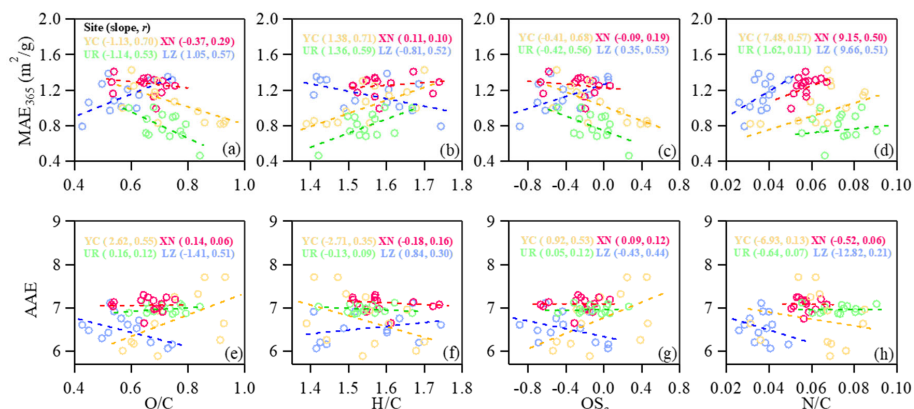Figure 9. (a) The mass spectra of PMF factors (WS-POA, HO-OOA1, HO-OOA2, LO-OOA), (b) correlations between PMF factors and various tracers, and (c) average contributions of WSOA factors to light absorption at 365 nm.
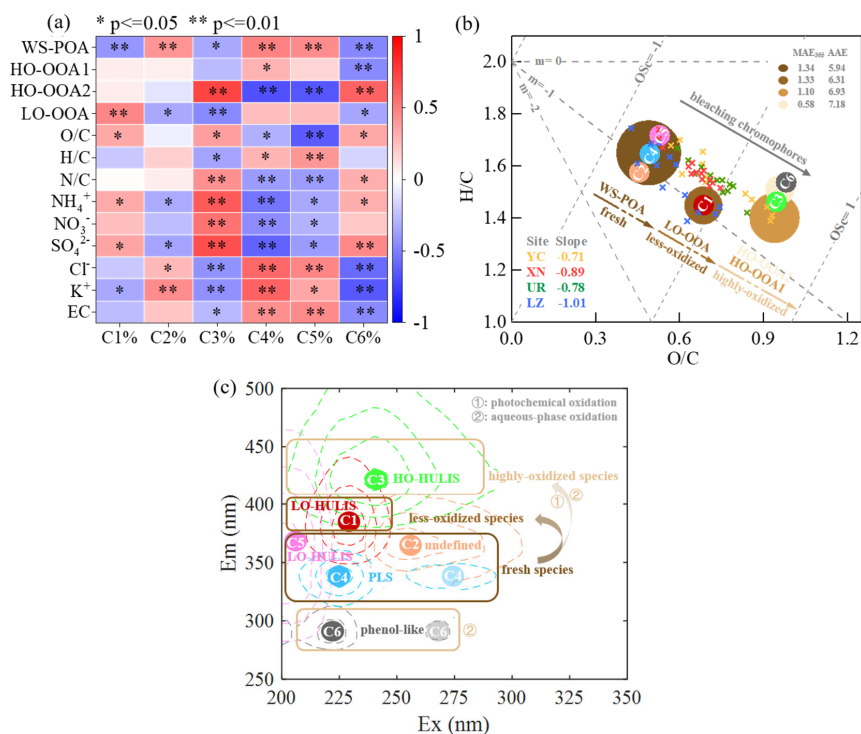
Figure 10. Scatter plots of MAE_{365} (a–d) and AAE (e–h) vs. (a, e) O/C, (b, f) H/C, (c, g) OS_c, and (d, h) N/C in four cities. The slope and correlation coefficient (*r*) by fitting the scatter of each group are shown, and p-test is significant at the 0.05 level when *r* reached 0.49.

Figure 11. The diagram illustrate the aging from fresh species to less oxidized and/or highly-oxidized species and corresponding variation on optical properties. (a) Heatmap of the correlation analysis between the PARAFAC components and PMF factors, with highly significant correlations (p < 0.01) are marked by** and significant correlations (0.01 < p < 0.05) marked by *. (b) The Van Krevelen plot (H:C vs. O:C) for ambient WSOA samples and different WSOA factors in this study,

with the slopes of the fitted line for ambient WSOA samples from each city noted in the lower left. The fitted MAE_{365} and AAE values for each WSOA factor are noted in the upper right, and each WSOA factor is colored by its MAE_{365} value, with fading color indicating bleaching chromophores. The size of the color block represents the average contribution of each WSOA factor to Abs_{365}. Based on the correlation coefficients between PARAFAC components and PMF factors, C2, C4, and C5 chromophores were assigned to WS-POA, C1 chromophore assigned to LO-OOA, and C3 and C6 chromophore assigned to HO-OOA (HO-OOA1 and HO-OOA2). (c) The Ex-Em plot for fluorescence peak positions (Ex/Em) and the corresponding compounds of these six fluorophores.

Tables

Table 1. Light-absorbing properties of BrC in $PM_{2.5}$ water extract in four cities.

	YC	XN	UR	LZ
Light absorption property				
AAE	6.81 ± 0.69	7.06 ± 0.44	6.94 ± 0.25	6.41 ± 0.51
Abs_{365} (M/m)	9.77 ± 4.74	12.03 ± 3.16	6.46 ± 1.60	12.49 ± 4.94
MAE_{365} (m^2/g)	1.02 ± 0.23	1.22 ± 0.18	0.78 ± 0.16	1.19 ± 0.12
MAE_{405} (m^2/g)	0.48 ± 0.14	0.57 ± 0.11	0.37 ± 0.09	0.59 ± 0.10
$f_{300-400}$ (%)	21.15 ± 5.62	22.47 ± 5.85	19.03 ± 5.17	25.17 ± 6.5
$f_{300-600}$ (%)	11.86 ± 2.92	12.44 ± 3.04	10.61 ± 2.64	14.11 ± 3.61